

# Dictionary-Free MRI PERK: Parameter Estimation via Regression with Kernels

Gopal Nataraj\*, *Student Member, IEEE*, Jon-Fredrik Nielsen,  
Clayton Scott, *Member, IEEE*, and Jeffrey A. Fessler, *Fellow, IEEE*

**Abstract**—This paper introduces a fast, general method for dictionary-free parameter estimation in quantitative magnetic resonance imaging (QMRI) via regression with kernels (PERK). PERK first uses prior distributions and the nonlinear MR signal model to simulate many parameter-measurement pairs. Inspired by machine learning, PERK then takes these parameter-measurement pairs as labeled training points and learns from them a nonlinear regression function using kernel functions and convex optimization. PERK admits a simple implementation as per-voxel nonlinear lifting of MRI measurements followed by linear minimum mean-squared error regression. We demonstrate PERK for  $T_1, T_2$  estimation, a well-studied application where it is simple to compare PERK estimates against dictionary-based grid search estimates. Numerical simulations as well as single-slice phantom and *in vivo* experiments demonstrate that PERK and grid search produce comparable  $T_1, T_2$  estimates in white and gray matter, but PERK is consistently at least  $23\times$  faster. This acceleration factor will increase by several orders of magnitude for full-volume QMRI estimation problems involving more latent parameters per voxel.

## I. INTRODUCTION

In quantitative magnetic resonance imaging (QMRI), one seeks to estimate latent parameter images from suitably informative data. Since MR acquisitions are tunably sensitive to many physical processes (*e.g.*, relaxation [1], diffusion [2], and chemical exchange [3]), MRI parameter estimation is important for many QMRI applications (*e.g.*, relaxometry [4], diffusion tensor imaging [5], and multi-compartmental imaging [6]). Motivated by widespread applications, this manuscript introduces a general method for fast MRI parameter estimation.

A common MRI parameter estimation strategy involves minimizing a cost function related to a statistical likelihood function. Because MR signal models are typically nonlinear functions of the underlying latent parameters, such likelihood-based estimation usually requires non-convex optimization. To seek good solutions, many recent works (*e.g.*, [7]–[16]) approach estimation with algorithms that employ exhaustive grid search, which requires either storing or computing on-the-fly

a “dictionary” of signal vectors. These works estimate a small number (2-3) of nonlinear latent parameters, so grid search is practical. However, for moderate or large sized problems, the required number of dictionary elements renders grid search undesirable or even intractable, unless one imposes artificially restrictive latent parameter constraints. Though several recent works [9], [12], [15], [16] focus on reducing dictionary storage requirements, all of these methods ultimately rely on some form of dictionary-based grid search.

There are numerous QMRI applications that could benefit from an alternative parameter estimation method that scales well with the number of latent parameters. For example, vector (*e.g.*, flow [17]) and tensor (*e.g.*, diffusivity [5] or conductivity [18]) field mapping techniques require estimation of at minimum 4 and 7 latent parameters per voxel, respectively. Phase-based longitudinal [19] or transverse [20], [21] field mapping could avoid noise-amplifying algebraic manipulations on reconstructed image data that are conventionally used to reduce signal dependencies on nuisance latent parameters. Compartmental fraction mapping [6], [22] from steady-state pulse sequences requires estimation of at least 7 [23] and as many as 10 [24] latent parameters per voxel. In these and other applications, greater estimation accuracy requires more complete signal models that involve more latent parameters, increasing the need for scalable estimation methods.

The fundamental challenge of scalable MRI parameter estimation stems from MR signal model nonlinearity: standard linear estimators would be scalable but inaccurate. One natural solution strategy involves nonlinearly preprocessing reconstructed images such that the transformed images are at least approximately linear in the latent parameters. As an example, for simple  $T_2$  estimation from measurements at multiple echo times, one could apply linear regression to the logarithm of the measurements. However, such simple transformations are generally not evident for more complicated signal models. Without such problem-specific insight, sufficiently rich nonlinear transformations could dramatically increase problem dimensionality, hindering scalability. Fortunately, a celebrated result in approximation theory [25] showed that simple transformations involving *reproducing kernel* functions [26] can represent nonlinear estimators whose evaluation need not directly scale in computation with the (possibly very high) dimension of the associated transformed data. These kernel methods later found popularity in machine learning (initially for classification [27] and quickly thereafter for other applications, *e.g.*, regression [28]) because they provided simple, scalable nonlinear extensions to fast linear algorithms.

This work was supported in part by the following grants: NIH grant P01 CA87634; a UM “MCubed” seed grant; and a UM predoctoral fellowship. *Asterisk indicates corresponding author.*

\*G. Nataraj, C. Scott, and J. A. Fessler are with the Department of Electrical Engineering and Computer Science, University of Michigan, Ann Arbor, MI, 48109, USA (email: gnataraj, @umich.edu).

J.-F. Nielsen is with the Department of Biomedical Engineering, University of Michigan, Ann Arbor, MI, 48109, USA (email: jfnielse@umich.edu).

C. Scott and J. A. Fessler are with the Department of Electrical Engineering and Computer Science, University of Michigan, Ann Arbor, MI, USA (email: {clayscot, fessler}@umich.edu).

This paper introduces<sup>1</sup> a scalable, dictionary-free method for MRI parameter estimation via regression with kernels (PERK). PERK first simulates many instances of latent parameter inputs and measurement outputs using prior distributions and the nonlinear MR signal model. PERK takes such input-output pairs as simulated *training points* and then *learns* (using an appropriate nonlinear kernel function) a nonlinear *regression function* from the training points. PERK will scale considerably better with the number of latent parameters than likelihood-based estimation via grid search.

The remainder of this manuscript is organized as follows. §II reviews pertinent background information about kernels. §III formulates a function optimization problem for MRI parameter estimation and efficiently solves this problem using kernels. §IV studies bias and covariance of the resulting PERK estimator. §V addresses practical implementation issues such as computational complexity and model selection. §VI demonstrates PERK in numerical simulations as well as phantom and *in vivo* experiments. §VII discusses advantages, challenges, and extensions. §VIII summarizes key contributions.

## II. PRELIMINARIES

This brief section reviews relevant definitions and facts about kernels. A (real-valued) *kernel*  $k : \mathbb{P}^2 \mapsto \mathbb{R}$  is a function that describes a measure of similarity between two pattern vectors  $\mathbf{p}, \mathbf{p}' \in \mathbb{P}$ . The matrix  $\mathbf{K} \in \mathbb{R}^{N \times N}$  associated with kernel  $k$  and  $N \in \mathbb{N}$  patterns  $\mathbf{p}_1, \dots, \mathbf{p}_N \in \mathbb{P}$  consists of entries  $k(\mathbf{p}_n, \mathbf{p}_{n'})$  for  $n, n' \in \{1, \dots, N\}$ . A *positive definite kernel* is a kernel for which  $\mathbf{K}$  is positive semidefinite (PSD) for any finite set of pattern vectors, in which case  $\mathbf{K}$  is a *Gram matrix*. A *symmetric kernel* satisfies  $k(\mathbf{p}, \mathbf{p}') = k(\mathbf{p}', \mathbf{p}) \forall \mathbf{p}, \mathbf{p}' \in \mathbb{P}$ . We hereafter restrict attention to symmetric, positive definite (SPD) kernels.

An SPD kernel  $k : \mathbb{P}^2 \mapsto \mathbb{R}$  defines an inner product in a particular Hilbert function space  $\bar{\mathbb{H}}$  that we briefly describe here because it characterizes the class of candidate regression functions over which PERK operates. To envision  $\bar{\mathbb{H}}$ , first define a kernel's associated (*canonical*) *feature map*  $\mathbf{z} : \mathbb{P} \mapsto \mathbb{R}^{\mathbb{P}}$  that assigns each  $\mathbf{p} \in \mathbb{P}$  to a (*canonical*) *feature*  $k(\cdot, \mathbf{p}) \in \mathbb{R}^{\mathbb{P}}$ . Then  $\bar{\mathbb{H}}$  is a completion of the space  $\mathbb{H} := \left\{ \sum_{n=1}^N a_n k(\cdot, \mathbf{p}_n) \right\}$  spanned by point evaluations of the feature map, where  $N \in \mathbb{N}$ ,  $a_1, \dots, a_N \in \mathbb{R}$ , and  $\mathbf{p}_1, \dots, \mathbf{p}_N \in \mathbb{P}$  are arbitrary. Let  $\langle \cdot, \cdot \rangle : \bar{\mathbb{H}}^2 \mapsto \mathbb{R}$  denote the inner product on  $\bar{\mathbb{H}}$ . Then for any  $h, h' \in \bar{\mathbb{H}}$  that have finite-dimensional canonical representations  $h := \sum_{n=1}^N a_n k(\cdot, \mathbf{p}_n)$  and  $h' := \sum_{n'=1}^N b_{n'} k(\cdot, \mathbf{p}_{n'})$ , the assignment

$$\langle h, h' \rangle_{\bar{\mathbb{H}}} = \sum_{n=1}^N \sum_{n'=1}^N a_n b_{n'} k(\mathbf{p}_{n'}, \mathbf{p}_n) \quad (1)$$

is consistent with the inner product on  $\bar{\mathbb{H}}$ . This inner product exhibits  $\forall h \in \bar{\mathbb{H}}, \mathbf{p} \in \mathbb{P}$  an interesting *reproducing property*

$$\langle h, k(\cdot, \mathbf{p}) \rangle_{\bar{\mathbb{H}}} = h(\mathbf{p}) \quad (2)$$

<sup>1</sup>This manuscript substantially extends [29], our conference paper that recently introduced kernel-based MRI parameter estimation. Though popular in the machine learning community, kernels had not (to our knowledge) been used prior to [29] for MRI parameter estimation.

that can be seen to directly follow from (1) for  $h \in \bar{\mathbb{H}}$ .

A *reproducing kernel* (RK) is a kernel that satisfies (2) for some real-valued Hilbert space  $\bar{\mathbb{H}}$ . A kernel is reproducing if and only if it is SPD. There is a bijection between RK  $k$  and  $\bar{\mathbb{H}}$ , and so  $\bar{\mathbb{H}}$  is often called the *reproducing kernel Hilbert space* (RKHS) uniquely associated with RK  $k$ . This bijection is critical to practical function optimization over an RKHS in that it translates inner products in a (usually high-dimensional) RKHS  $\bar{\mathbb{H}}$  into equivalent kernel operations in the (lower-dimensional) pattern vector space  $\mathbb{P}$ . The following sections exploit the bijection between an RKHS and its associated RK.

## III. A FUNCTION OPTIMIZATION PROBLEM AND KERNEL SOLUTION FOR MRI PARAMETER ESTIMATION

After image reconstruction, many QMRI acquisitions produce at each voxel position a sequence of noisy measurements  $\mathbf{y} \in \mathbb{C}^D$ , modeled as

$$\mathbf{y} = \mathbf{s}(\mathbf{x}, \boldsymbol{\nu}) + \boldsymbol{\epsilon}, \quad (3)$$

where  $\mathbf{x} \in \mathbb{R}^L$  denotes  $L$  *latent* parameters (*e.g.*, relaxation time constants);  $\boldsymbol{\nu} \in \mathbb{R}^K$  denotes  $K$  *known* parameters (*e.g.*, separately acquired and estimated field maps);  $\mathbf{s} : \mathbb{R}^L \times \mathbb{R}^K \mapsto \mathbb{C}^D$  models noiseless signals that arise from  $D$  datasets and is a continuous function in its arguments; and  $\boldsymbol{\epsilon} \in \mathbb{C}^D$  is noise with known distribution (we assume  $\boldsymbol{\epsilon} \sim \mathcal{CN}(\mathbf{0}_D, \boldsymbol{\Sigma})$  with zero mean  $\mathbf{0}_D \in \mathbb{R}^D$  and known covariance  $\boldsymbol{\Sigma} \in \mathbb{R}^{D \times D}$ ). We seek to estimate on a per-voxel basis each latent parameter  $\mathbf{x}$  from corresponding measurement  $\mathbf{y}$  and known parameter  $\boldsymbol{\nu}$ .

To develop an estimator  $\hat{\mathbf{x}}$ , we simulate many instances of forward model (3) and use kernels to estimate a nonlinear inverse function. We sample part of  $\mathbb{R}^L \times \mathbb{R}^K \times \mathbb{C}^D$  and evaluate (3)  $N$  times to produce sets of parameter and noise realizations  $\{(\mathbf{x}_1, \boldsymbol{\nu}_1, \boldsymbol{\epsilon}_1), \dots, (\mathbf{x}_N, \boldsymbol{\nu}_N, \boldsymbol{\epsilon}_N)\}$  and corresponding measurements  $\{\mathbf{y}_1, \dots, \mathbf{y}_N\}$ . We seek a function  $\hat{\mathbf{h}} : \mathbb{R}^P \mapsto \mathbb{R}^L$  and an offset  $\hat{\mathbf{b}} \in \mathbb{R}^L$  that together map each pure-real<sup>2</sup> regressor  $\mathbf{p}_n := [|\mathbf{y}_n|^\top, \boldsymbol{\nu}_n^\top]^\top$  to an estimate  $\hat{\mathbf{x}}(\mathbf{p}_n) := \hat{\mathbf{h}}(\mathbf{p}_n) + \hat{\mathbf{b}}$  that is “close” to corresponding regressand  $\mathbf{x}_n$ , where  $P := D + K$ ,  $n \in \{1, \dots, N\}$ , and  $(\cdot)^\top$  denotes vector transpose. For any finite  $N$ , there are infinitely many candidate estimators that are consistent with training points in this manner. We use function regularization to choose one estimator that smoothly interpolates between training points:

$$\left( \hat{\mathbf{h}}, \hat{\mathbf{b}} \right) \in \arg \min_{\substack{\mathbf{h} \in \bar{\mathbb{H}}^L \\ \mathbf{b} \in \mathbb{R}^L}} \Psi(\mathbf{h}, \mathbf{b}; \{(\mathbf{x}_n, \mathbf{p}_n)\}_1^N), \text{ where} \quad (4)$$

$$\Psi(\dots) = \sum_{l=1}^L \Psi_l(h_l, b_l; \{(x_{l,n}, \mathbf{p}_n)\}_1^N); \quad (5)$$

$$\Psi_l(\dots) = \rho_l \|h_l\|_{\bar{\mathbb{H}}}^2 + \frac{1}{N} \sum_{n=1}^N (h_l(\mathbf{p}_n) + b_l - x_{l,n})^2. \quad (6)$$

Here, each  $h_l : \mathbb{R}^P \mapsto \mathbb{R}$  is a scalar function that maps to the  $l$ th component of the output of  $\mathbf{h}$ ; each  $b_l, x_{l,n} \in \mathbb{R}$  are

<sup>2</sup>We present our methodology assuming pure-real patterns  $\mathbf{p}$  and estimators  $\hat{\mathbf{x}}$  for simplicity and to maintain consistency with experiments, in which we choose to use magnitude images for unrelated reasons (see §VI.A for details). It is straightforward to generalize Theorem 1 for complex-valued kernels and thereby address the cases of complex patterns and/or estimators.

scalar components of  $\mathbf{b}, \mathbf{x}_n$ ;  $\mathbb{H}$  is an RKHS whose norm  $\|\cdot\|_{\mathbb{H}}$  is induced by inner product  $\langle \cdot, \cdot \rangle_{\mathbb{H}} : \mathbb{H}^2 \mapsto \mathbb{R}$ ; and each  $\rho_l$  controls for regularity in  $h_l$ .

Since (5) is separable in the components of  $\mathbf{h}$  and  $\mathbf{b}$ , it suffices to consider optimizing each  $(h_l, b_l)$  by separately minimizing (6) for each  $l \in \{1, \dots, L\}$ . Remarkably, a generalization of the Representer Theorem [30], restated as is relevant here for completeness, reduces minimizing (6) to a finite-dimensional optimization problem.

**Theorem 1** (Generalized Representer, [30]). *Define  $k : \mathbb{R}^Q \times \mathbb{R}^Q \mapsto \mathbb{R}$  to be the SPD kernel associated with RKHS  $\mathbb{H}$ , such that reproducing property  $h_l(\mathbf{p}) = \langle h_l, k(\cdot, \mathbf{p}) \rangle_{\mathbb{H}}$  holds for all  $h_l \in \mathbb{H}$  and  $\mathbf{p} \in \mathbb{R}^Q$ . Then any minimizer  $(\hat{h}_l, \hat{b}_l)$  of (6) over  $\mathbb{H} \times \mathbb{R}$  admits a representation for  $\hat{h}_l$  of the form*

$$\hat{h}_l(\cdot) \equiv \sum_{n=1}^N a_{l,n} k(\cdot, \mathbf{p}_n), \quad (7)$$

where each  $a_{l,n} \in \mathbb{R}$  for  $n \in \{1, \dots, N\}$ .

Theorem 1 ensures that any solution to the component-wise  $(N+1)$ -dimensional problem

$$\begin{aligned} (\hat{\mathbf{a}}_l, \hat{b}_l) \in \arg \min_{\substack{\mathbf{a}_l \in \mathbb{R}^N \\ b_l \in \mathbb{R}}} \rho_l \left\| \sum_{n'=1}^N a_{l,n'} k(\cdot, \mathbf{p}_{n'}) \right\|_{\mathbb{H}}^2 + \\ \frac{1}{N} \sum_{n=1}^N \left( \sum_{n'=1}^N a_{l,n'} k(\mathbf{p}_n, \mathbf{p}_{n'}) + b_l - x_{l,n} \right)^2 \end{aligned} \quad (8)$$

corresponds via (7) to a minimizer of (6) over  $\mathbb{H} \times \mathbb{R}$ , where  $\mathbf{a}_l := [a_{l,1}, \dots, a_{l,N}]^T$ . Fortunately, a solution of (8) exists uniquely for  $\rho_l > 0$  and can be expressed as

$$\hat{\mathbf{a}}_l = (\mathbf{MKM} + N\rho_l \mathbf{I}_N)^{-1} \mathbf{M} \mathbf{x}_l; \quad (9)$$

$$\hat{b}_l = \frac{1}{N} \mathbf{1}_N^T (\mathbf{x}_l - \mathbf{K} \hat{\mathbf{a}}_l), \quad (10)$$

where  $\mathbf{K} \in \mathbb{R}^{N \times N}$  is the Gram matrix consisting of entries  $k(\mathbf{p}_n, \mathbf{p}_{n'})$  for  $n, n' \in \{1, \dots, N\}$ ;  $\mathbf{M} := \mathbf{I}_N - \frac{1}{N} \mathbf{1}_N \mathbf{1}_N^T \in \mathbb{R}^{N \times N}$  is a de-meaning operator;  $\mathbf{x}_l := [x_{l,1}, \dots, x_{l,N}]^T$ ;  $\mathbf{I}_N \in \mathbb{R}^{N \times N}$  is the identity matrix; and  $\mathbf{1}_N \in \mathbb{R}^N$  is a vector of ones. Substituting (9) into (7) yields an expression for the  $l$ th entry  $\hat{x}_l$  of MRI parameter estimator  $\hat{\mathbf{x}}$ :

$$\hat{x}_l(\cdot) \leftarrow \mathbf{x}_l^T \left( \frac{1}{N} \mathbf{1}_N + \mathbf{M} (\mathbf{MKM} + N\rho_l \mathbf{I}_N)^{-1} \mathbf{k}(\cdot) \right), \quad (11)$$

where  $\mathbf{k}(\cdot) := [k(\cdot, \mathbf{p}_1), \dots, k(\cdot, \mathbf{p}_N)]^T - \frac{1}{N} \mathbf{K} \mathbf{1}_N : \mathbb{R}^Q \mapsto \mathbb{R}^N$  is a kernel embedding operator.

When  $\rho_l > 0 \forall l \in \{1, \dots, L\}$ , estimator  $\hat{\mathbf{x}}(\cdot)$  with entries (11) minimizes (5) over  $\mathbb{H}^L \times \mathbb{R}^L$ . However, the utility of  $\hat{\mathbf{x}}(\cdot)$  depends on the choice of kernel  $k$ , which induces a choice on the RKHS  $\mathbb{H}$  and thus the function space  $\mathbb{H}^L \times \mathbb{R}^L$  over which (4) optimizes. For example, if  $k$  was selected as the canonical dot product  $k(\mathbf{p}, \mathbf{p}') \leftarrow \langle \mathbf{p}, \mathbf{p}' \rangle_{\mathbb{R}^Q} := \mathbf{p}^T \mathbf{p}'$  (for which RKHS  $\mathbb{H} \leftarrow \mathbb{R}^Q$ ), then (11) would reduce to affine ridge regression [31] which is optimal over  $\mathbb{R}^Q \times \mathbb{R}$  but is unlikely to be useful when signal model  $\mathbf{s}$  is nonlinear in  $\mathbf{x}$ . Since we expect a useful estimate  $\hat{\mathbf{x}}(\mathbf{p})$  to depend nonlinearly (but smoothly) on  $\mathbf{p}$  in general, we instead use an SPD kernel  $k$  that is likewise

nonlinear in its arguments and thus corresponds to an RKHS much richer than  $\mathbb{R}^Q$ . Specifically, we use a Gaussian kernel

$$k(\mathbf{p}, \mathbf{p}') \leftarrow \exp \left( -\frac{1}{2} \|\mathbf{p} - \mathbf{p}'\|_{\Lambda^{-2}}^2 \right), \quad (12)$$

where positive definite matrix bandwidth  $\Lambda \in \mathbb{R}^{Q \times Q}$  controls the length scales in  $\mathbf{p}$  over which the estimator  $\hat{\mathbf{x}}$  smooths and  $\|\cdot\|_{\Gamma} \equiv \|\Gamma^{1/2}(\cdot)\|_2$  is a weighted  $\ell^2$ -norm with PSD matrix weights  $\Gamma$ . We use a Gaussian kernel over other candidates because it is a *universal kernel*, meaning weighted sums of the form  $\sum_{n=1}^N a_n k(\cdot, \mathbf{p}_n)$  can approximate  $\mathcal{L}^2$  functions to arbitrary accuracy for  $N$  sufficiently large [32].

Interestingly, the RKHS associated with Gaussian kernel (12) is infinite-dimensional. Thus, Gaussian kernel regression can be interpreted as first “lifting” via a nonlinear *feature map*  $\mathbf{z} : \mathbb{R}^Q \mapsto \mathbb{H}$  each  $\mathbf{p}$  into an infinite-dimensional *feature*  $\mathbf{z}(\mathbf{p}) = k(\cdot, \mathbf{p}) \in \mathbb{H}$ , and then performing regularized affine regression on the features via dot products of the form  $\langle k(\cdot, \mathbf{p}), k(\cdot, \mathbf{p}') \rangle_{\mathbb{H}} = k(\mathbf{p}', \mathbf{p})$ . From this perspective, the challenges of nonlinear estimation via likelihood models are avoided because we *select* (through the choice of kernel) characteristics of the nonlinear dependence that we wish to model and need only *estimate* via (8) the linear dependence of each entry in  $\hat{\mathbf{x}}$  on the corresponding features.

#### IV. BIAS AND COVARIANCE ANALYSIS

This section presents expressions for the bias and covariance of Gaussian PERK estimator  $\hat{\mathbf{x}}(\cdot)$ , conditioned on object parameters  $\mathbf{x}, \boldsymbol{\nu}$ . We focus on these conditional statistics to enable study of estimator performance as  $\mathbf{x}, \boldsymbol{\nu}$  are varied. Though not mentioned explicitly hereafter, both expressions treat the training sample  $\{(\mathbf{x}_1, \mathbf{p}_1), \dots, (\mathbf{x}_N, \mathbf{p}_N)\}$  and regularization parameters  $\rho_1, \dots, \rho_L$  as fixed.

##### A. Conditional Bias

The conditional bias of  $\hat{\mathbf{x}} \equiv \hat{\mathbf{x}}(\boldsymbol{\alpha}, \boldsymbol{\nu})$  is written as

$$\begin{aligned} \text{bias}(\hat{\mathbf{x}}|\mathbf{x}, \boldsymbol{\nu}) &:= \mathbb{E}_{\boldsymbol{\alpha}|\mathbf{x}, \boldsymbol{\nu}}(\hat{\mathbf{x}}(\boldsymbol{\alpha}, \boldsymbol{\nu})) - \mathbf{x} \\ &= \mathbf{R} \mathbb{E}_{\boldsymbol{\alpha}|\mathbf{x}, \boldsymbol{\nu}}(\mathbf{k}(\boldsymbol{\alpha}, \boldsymbol{\nu})) + (\mathbf{m}_{\mathbf{x}} - \mathbf{x}), \end{aligned} \quad (13)$$

where  $\mathbb{E}_{\boldsymbol{\alpha}|\mathbf{x}, \boldsymbol{\nu}}(\cdot)$  denotes expectation with respect to  $\boldsymbol{\alpha} := |\mathbf{y}|$  and conditioned on  $\mathbf{x}, \boldsymbol{\nu}$ . Here, the  $l$ th row of  $\mathbf{R} \in \mathbb{R}^{L \times N}$  and  $l$ th entry of regressand sample mean  $\mathbf{m}_{\mathbf{x}} \in \mathbb{R}^L$  respectively are  $\mathbf{x}_l^T \mathbf{M} (\mathbf{MKM} + N\rho_l \mathbf{I}_N)^{-1}$  and  $\frac{1}{N} \mathbf{x}_l^T \mathbf{1}_N$  for  $l \in \{1, \dots, L\}$ . To proceed analytically, we make two mild assumptions. First, we assume that  $\mathbf{y} \sim \mathcal{CN}(\mathbf{0}_D, \boldsymbol{\Sigma})$  has sufficiently high signal-to-noise ratio (SNR) such that its complex modulus  $\boldsymbol{\alpha}$  is approximately Gaussian-distributed. We specifically consider the typical case where covariance matrix  $\boldsymbol{\Sigma}$  is diagonal with diagonal entries  $\sigma_1^2, \dots, \sigma_D^2$ , in which case measurement amplitude conditional distribution  $p_{\boldsymbol{\alpha}|\mathbf{x}, \boldsymbol{\nu}}$  is simply approximated as  $p_{\boldsymbol{\alpha}|\mathbf{x}, \boldsymbol{\nu}} \leftarrow \mathcal{N}(\boldsymbol{\mu}, \boldsymbol{\Sigma})$ , where  $\boldsymbol{\mu} \in \mathbb{R}^D$  has  $d$ th coordinate  $\sqrt{|s_d(\mathbf{x}, \boldsymbol{\nu})|^2 + \sigma_d^2}$  for  $d \in \{1, \dots, D\}$  [33]. Second, we assume that the Gaussian kernel bandwidth matrix  $\Lambda$  has the block diagonal structure

$$\Lambda \leftarrow \begin{bmatrix} \Lambda_{\boldsymbol{\alpha}} & \mathbf{0}_{D \times K} \\ \mathbf{0}_{K \times D} & \Lambda_{\boldsymbol{\nu}} \end{bmatrix} \quad (14)$$

where  $\Lambda_\alpha \in \mathbb{R}^{D \times D}$  and  $\Lambda_\nu \in \mathbb{R}^{K \times K}$  are positive definite. With these simplifying assumptions, the  $n$ th entry of the expectation in (13) is well approximated as  $[\mathbb{E}_{\alpha|\mathbf{x}, \nu}(\mathbf{k}(\alpha, \nu))]_n$

$$\begin{aligned} &= \int_{\mathbb{R}^D} e^{-\frac{1}{2}\|\mathbf{p}-\mathbf{p}_n\|_{\Lambda_\alpha^{-2}}^2} \mathbf{p}_{\alpha|\mathbf{x}, \nu}(\alpha|\mathbf{x}, \nu) \, d\alpha \\ &\approx \frac{e^{-\frac{1}{2}\|\nu-\nu_n\|_{\Lambda_\nu^{-2}}^2}}{\sqrt{(2\pi)^D \det(\Sigma)}} \int_{\mathbb{R}^D} e^{-\frac{1}{2}\left(\|\alpha-\alpha_n\|_{\Lambda_\alpha^{-2}}^2 + \|\alpha-\mu\|_{\Sigma^{-1}}^2\right)} \, d\alpha \\ &= \frac{e^{-\frac{1}{2}\left(\|\nu-\nu_n\|_{\Lambda_\nu^{-2}}^2 + \|\mu-\alpha_n\|_{(\Lambda_\alpha^{-2}\Sigma + \mathbf{I}_D)^{-1}\Lambda_\alpha^{-2}}^2\right)}}{\sqrt{\det(\Lambda_\alpha^{-2}\Sigma + \mathbf{I}_D)}}, \end{aligned} \quad (15)$$

where  $\det(\cdot)$  denotes determinant and the Gaussian integral follows after completing the square of the integrand's exponent. It is clear from (15) that as  $\Sigma \rightarrow \mathbf{0}_{D \times D}$  for fixed  $\Lambda_\alpha$ ,  $\mathbb{E}_{\alpha|\mathbf{x}, \nu}(\mathbf{k}(\alpha, \nu)) \rightarrow \mathbf{k}(\mu, \nu)$  and therefore

$$\mathbb{E}_{\alpha|\mathbf{x}, \nu}(\widehat{\mathbf{x}}(\alpha, \nu)) \rightarrow \widehat{\mathbf{x}}(\mathbb{E}_{\alpha|\mathbf{x}, \nu}(\alpha), \nu) \equiv \widehat{\mathbf{x}}(\mu, \nu) \quad (16)$$

which perhaps surprisingly means that the conditional bias asymptotically approaches the noiseless conditional estimation error  $\widehat{\mathbf{x}}(\mu, \nu) - \mathbf{x}$  despite  $\widehat{\mathbf{x}}$  being nonlinear in  $\alpha$ .

### B. Conditional Covariance

The conditional covariance of  $\widehat{\mathbf{x}} \equiv \widehat{\mathbf{x}}(\alpha, \nu)$  is written as

$$\begin{aligned} \text{cov}(\widehat{\mathbf{x}}|\mathbf{x}, \nu) &:= \mathbb{E}_{\alpha|\mathbf{x}, \nu} \left( (\widehat{\mathbf{x}} - \mathbb{E}_{\alpha|\mathbf{x}, \nu}(\widehat{\mathbf{x}})) (\widehat{\mathbf{x}} - \mathbb{E}_{\alpha|\mathbf{x}, \nu}(\widehat{\mathbf{x}}))^T \right) \\ &= \mathbf{R} \mathbb{E}_{\alpha|\mathbf{x}, \nu} \left( \widetilde{\mathbf{k}}(\alpha, \nu) \widetilde{\mathbf{k}}(\alpha, \nu)^T \right) \mathbf{R}^T, \end{aligned} \quad (17)$$

where  $\widetilde{\mathbf{k}}(\alpha, \nu) := \mathbf{k}(\alpha, \nu) - \mathbb{E}_{\alpha|\mathbf{x}, \nu}(\mathbf{k}(\alpha, \nu))$ . To proceed analytically, we take the same high-SNR and block-diagonal bandwidth assumptions as in §IV.A. Then after straightforward manipulations similar to those yielding (15), the  $(n, n')$ th entry of the expectation in (17) is well approximated as

$$\begin{aligned} & \left[ \mathbb{E}_{\alpha|\mathbf{x}, \nu} \left( \widetilde{\mathbf{k}}(\alpha, \nu) \widetilde{\mathbf{k}}(\alpha, \nu)^T \right) \right]_{n, n'} \\ &= e^{-\frac{1}{2}\left(\|\nu-\nu_n\|_{\Lambda_\nu^{-2}}^2 + \|\nu-\nu_{n'}\|_{\Lambda_\nu^{-2}}^2\right)} \\ & \quad \times \left( \frac{e^{-\frac{1}{2}\left(\|\widetilde{\alpha}_n - \widetilde{\alpha}_{n'}\|_{\Delta(0)}^2 + \|\widetilde{\alpha}_n + \widetilde{\alpha}_{n'}\|_{\Delta(2)}^2\right)}}{\sqrt{\det(2\Lambda_\alpha^{-2}\Sigma + \mathbf{I}_D)}} \right. \\ & \quad \left. - \frac{e^{-\frac{1}{2}\left(\|\widetilde{\alpha}_n - \widetilde{\alpha}_{n'}\|_{\Delta(1)}^2 + \|\widetilde{\alpha}_n + \widetilde{\alpha}_{n'}\|_{\Delta(1)}^2\right)}}{\det(\Lambda_\alpha^{-2}\Sigma + \mathbf{I}_D)} \right), \end{aligned} \quad (18)$$

where  $\widetilde{\alpha}_n := \mu - \alpha_n$  and  $\Delta(t) := \frac{1}{2}(t\Lambda_\alpha^{-2}\Sigma + \mathbf{I}_D)^{-1}\Lambda_\alpha^{-2}$  for  $t \in \mathbb{N}$ . The emergence of  $\widetilde{\alpha}_n \pm \widetilde{\alpha}_{n'}$  terms in (18) show that the conditional covariance (unlike the conditional bias) is directly influenced not only by the individual expected test point distances to each of the training points  $\widetilde{\alpha}_1, \dots, \widetilde{\alpha}_N$  but also by the local training point sampling density.

## V. IMPLEMENTATION CONSIDERATIONS

This section focuses on important practical implementation issues. §V.A discusses a conceptually intuitive approximation of PERK estimator (11) that in many problems can significantly improve computational performance. §V.B describes strategies for data-driven model selection.

### A. A Kernel Approximation

In practical problems with even moderately large ambient dimension  $P$ , the necessarily large number of training samples  $N$  complicates storage of (dense)  $N \times N$  Gram matrix  $\mathbf{K}$ . Using a kernel approximation can mitigate storage and processing issues. Here we employ *random Fourier features* [34], a recent method for approximating translation-invariant kernels having form  $k(\mathbf{p}, \mathbf{p}') \equiv k(\mathbf{p} - \mathbf{p}')$ . This subsection reviews the main result of [34] for the purpose of constructing an intuitive and computationally efficient approximation of (11).

The strategy of [34] is to construct independent probability distributions  $\mathbf{p}_\nu$  and  $\mathbf{p}_s$  associated with random  $\mathbf{v} \in \mathbb{R}^P$  and random  $s \in \mathbb{R}$  as well as a function (that is parameterized by  $\mathbf{p}$ )  $\tilde{z}(\cdot, \cdot; \mathbf{p}) : \mathbb{R}^P \times \mathbb{R} \times \mathbb{R}^P \mapsto \mathbb{R}$ , such that

$$\mathbb{E}_{\mathbf{v}, s}(\tilde{z}(\mathbf{v}, s; \mathbf{p}) \tilde{z}(\mathbf{v}, s; \mathbf{p}')) = k(\mathbf{p} - \mathbf{p}'), \quad (19)$$

where  $\mathbb{E}_{\mathbf{v}, s}(\cdot)$  denotes expectation with respect to  $\mathbf{p}_\nu \mathbf{p}_s$ . When such a construction exists, one can build approximate feature maps  $\tilde{\mathbf{z}}$  by concatenating and normalizing evaluations of  $\tilde{z}$  on  $Z$  samples  $\{(\mathbf{v}_1, s_1), \dots, (\mathbf{v}_Z, s_Z)\}$  of  $(\mathbf{v}, s)$  (drawn jointly albeit independently), to produce approximate features

$$\tilde{\mathbf{z}}(\mathbf{p}) := \sqrt{\frac{2}{Z}} [\tilde{z}(\mathbf{v}_1, s_1; \mathbf{p}), \dots, \tilde{z}(\mathbf{v}_Z, s_Z; \mathbf{p})]^T \quad (20)$$

for any  $\mathbf{p}$ . Then by the strong law of large numbers,

$$\lim_{Z \rightarrow \infty} \langle \tilde{\mathbf{z}}(\mathbf{p}), \tilde{\mathbf{z}}(\mathbf{p}') \rangle_{\mathbb{R}^Z} \xrightarrow{a.s.} k(\mathbf{p}, \mathbf{p}') \quad \forall \mathbf{p}, \mathbf{p}' \quad (21)$$

which, in conjunction with strong performance guarantees for finite  $Z$  [34], [35], justifies interpreting  $\tilde{\mathbf{z}}$  as an approximate (and now finite-dimensional) feature map.

We use the Fourier construction of [34] that assigns  $\tilde{z}(\mathbf{v}, s; \mathbf{p}) \leftarrow \cos(2\pi(\mathbf{v}^T \mathbf{p} + s))$ . If also  $\mathbf{p}_s \leftarrow \text{unif}(0, 1)$ , then  $\mathbb{E}_{\mathbf{v}, s}(\tilde{z}(\mathbf{v}, s; \mathbf{p}) \tilde{z}(\mathbf{v}, s; \mathbf{p}'))$  simplifies to

$$\int_{\mathbb{R}^P} \cos(2\pi \mathbf{v}^T (\mathbf{p} - \mathbf{p}')) \mathbf{p}_\nu(\mathbf{v}) \, d\mathbf{v}. \quad (22)$$

For symmetric  $\mathbf{p}_\nu$ , (22) exists [36] and is a Fourier transform. Thus choosing  $\mathbf{p}_\nu \leftarrow \mathcal{N}(\mathbf{0}_P, (2\pi\Lambda)^{-2})$  satisfies (19) for Gaussian kernel (12), where  $\mathbf{0}_P \in \mathbb{R}^P$  is a vector of zeros.

Sampling  $\mathbf{p}_\nu, \mathbf{p}_s$   $Z$  times and subsequently constructing  $\tilde{\mathbf{Z}} := [\tilde{\mathbf{z}}(\mathbf{p}_1), \dots, \tilde{\mathbf{z}}(\mathbf{p}_N)] \in \mathbb{R}^{Z \times N}$  via repeated evaluations of (20) gives for  $Z \ll N$  a low-rank approximation  $\tilde{\mathbf{Z}}^T \tilde{\mathbf{Z}}$  of Gram matrix  $\mathbf{K}$ . Substituting this approximation into (11) and applying the matrix inversion lemma [37] yields

$$\widehat{\mathbf{x}}_l(\cdot) \leftarrow m_{x_l} + \mathbf{c}_{\mathbf{z}x_l}^T (\mathbf{C}_{\tilde{\mathbf{z}}\tilde{\mathbf{z}}} + \rho_l \mathbf{I}_Z)^{-1} (\tilde{\mathbf{z}}(\cdot) - \mathbf{m}_{\tilde{\mathbf{z}}}), \quad (23)$$

where  $m_{x_l} := \frac{1}{N} \mathbf{x}_l^T \mathbf{1}_N$  and  $\mathbf{m}_{\tilde{\mathbf{z}}} := \frac{1}{N} \tilde{\mathbf{Z}} \mathbf{1}_N$  are sample means; and  $\mathbf{c}_{\mathbf{z}x_l} := \frac{1}{N} \tilde{\mathbf{Z}} \mathbf{M} \mathbf{x}_l$  and  $\mathbf{C}_{\tilde{\mathbf{z}}\tilde{\mathbf{z}}} := \frac{1}{N} \tilde{\mathbf{Z}} \mathbf{M} \tilde{\mathbf{Z}}^T$  are sample covariances. Estimator (23) is an affine minimum mean-squared error estimator on the approximate features, and illustrates that Gaussian PERK via estimator (11) is asymptotically (in  $Z$ ) equivalent to regularized affine regression after nonlinear, high-dimensional feature mapping.

## B. Tuning Parameter Selection

This subsection proposes guidelines for data-driven selection of user-selectable parameters. Our goal here is to use problem intuition to automatically choose as many tuning parameters as possible, thereby leaving as few parameters as possible to manual selection. In this spirit, we focus on “on-line” model selection, where one chooses tuning parameters for training the estimator  $\widehat{\mathbf{x}}(\cdot)$  after acquiring (unlabeled) real test data. This online approach can be considered a form of *transductive learning* [38, Ch. 8] since we train our estimator with knowledge of unlabeled test data in addition to labeled training data. Observe that since many voxel-wise separable MRI parameter estimation problems are comparatively low-dimensional, PERK estimators can be quickly trained using only a moderate number of simulated training examples; in fact, training often takes less time than evaluating the PERK estimator on full-volume high-resolution measurement images. For these reasons, online PERK model selection is practical.

1) *Choosing Sampling Distribution*: For reasonable PERK performance, it is important to choose the joint distribution of latent and known parameters  $\mathbf{p}_{\mathbf{x},\nu}$  such that latent parameters can be estimated precisely over the joint distribution’s support  $\text{supp}(\mathbf{p}_{\mathbf{x},\nu})$ . For continuously differentiable magnitude signal model  $\mu$ , we quantify precision at a single point  $(\mathbf{x}, \nu)$  using the Fisher information matrix

$$\begin{aligned} \mathbf{F}(\mathbf{x}, \nu) &:= \mathbb{E}_{\alpha|\mathbf{x},\nu} \left( (\nabla_{\mathbf{x}} \log p_{\alpha|\mathbf{x},\nu})^{\top} \nabla_{\mathbf{x}} \log p_{\alpha|\mathbf{x},\nu} \right) \\ &\approx (\nabla_{\mathbf{x}} \mu(\mathbf{x}, \nu))^{\top} \Sigma^{-1} \nabla_{\mathbf{x}} \mu(\mathbf{x}, \nu) \end{aligned} \quad (24)$$

where  $\nabla_{\mathbf{x}}(\cdot)$  denotes row gradient with respect to  $\mathbf{x}$  and the approximation holds well for moderately high-SNR measurements [33]. When it exists, the inverse of  $\mathbf{F}(\mathbf{x}, \nu)$  provides a lower-bound on the conditional covariance of any unbiased estimator of  $\mathbf{x}$  [39]. For good performance, it is thus reasonable to ensure  $\mathbf{F}(\mathbf{x}, \nu)$  is well-conditioned over  $\text{supp}(\mathbf{p}_{\mathbf{x},\nu})$ .

There are many strategies one could employ to control the condition number of  $\mathbf{F}(\mathbf{x}, \nu)$  over  $\text{supp}(\mathbf{p}_{\mathbf{x},\nu})$ . In our experiments, we used data [14] from acquisitions designed to *minimize* a cost function related to the *maximum* of  $\mathbf{F}^{-1}(\mathbf{x}, \nu)$  over bounded latent and known parameter ranges of interest (§VI.A provides application-specific details). We then assigned  $\text{supp}(\mathbf{p}_{\mathbf{x},\nu})$  to coincide with the support of these acquisition design parameter ranges of interest. Assessing worst-case imprecision via the conservative minimax criterion is appropriate here because point-wise poor conditioning at any  $(\mathbf{x}, \nu) \in \text{supp}(\mathbf{p}_{\mathbf{x},\nu})$  can induce PERK estimation error over larger subsets of  $\text{supp}(\mathbf{p}_{\mathbf{x},\nu})$ .

If many separate prior parameter estimates are available, one can estimate the particular shape of  $\mathbf{p}_{\mathbf{x},\nu}$  empirically and then clip and renormalize  $\mathbf{p}_{\mathbf{x},\nu}$  so as to assign nonzero probability only within an appropriate support. When prior estimates are unavailable, it may in certain problems be reasonable to instead assume a separable distributional structure  $\mathbf{p}_{\mathbf{x},\nu} \equiv \mathbf{p}_{\mathbf{x}} \mathbf{p}_{\nu}$  in which case one can still estimate  $\mathbf{p}_{\nu}$  empirically but must set  $\mathbf{p}_{\mathbf{x}}$  manually based on typical ranges of latent parameters.

2) *Choosing Regularization Parameters*: As presented, PERK estimator (11) and its approximation (23) leave freedom to select different regularization parameters  $\rho_1, \dots, \rho_L$  for

estimating each of the  $L$  latent parameters. However, the respective unitless matrices  $\mathbf{M}\mathbf{K}\mathbf{M}$  and  $\mathbf{C}_{\mathbf{z}\mathbf{z}}$  whose condition numbers are influenced by  $\rho_1, \dots, \rho_L$  do not vary with  $l$ . Thus it is reasonable to assign each  $\rho_l \leftarrow \rho \forall l \in \{1, \dots, L\}$  some fixed  $\rho > 0$ . This simplification significantly reduces training computation to just one rather than  $L$  large matrix inversions. We select the scalar regularization parameter  $\rho$  using the holdout process described in §S.I.

3) *Choosing Kernel Bandwidth*: It is desirable to choose the Gaussian kernel’s bandwidth matrix  $\mathbf{\Lambda}$  such that PERK estimates are invariant to the overall scale of test data. We use (after observing test data, and for both training and testing)

$$\mathbf{\Lambda} \leftarrow \lambda \text{diag} \left( [\mathbf{m}_{\alpha}^{\top}, \mathbf{m}_{\nu}^{\top}]^{\top} \right), \quad (25)$$

where  $\mathbf{m}_{\alpha} \in \mathbb{R}^D$  and  $\mathbf{m}_{\nu} \in \mathbb{R}^K$  are sample means across voxels of magnitude test image data and known parameters, respectively; and  $\text{diag}(\cdot)$  assigns its argument to the diagonal entries of an otherwise zero matrix. We select the only scalar bandwidth parameter  $\lambda > 0$  using holdout as well.

## VI. EXPERIMENTATION

This section demonstrates PERK for quantifying MR relaxation parameters  $T_1$  and  $T_2$ , a well-studied application. We studied this relatively simple problem instead of the more complicated problems that motivated our method because we had access to reference  $T_1, T_2$  phantom NMR measurements [40] for external validation and because it is easier to validate PERK estimates against gold-standard grid search estimates in problems involving few unknowns. §VI.A describes implementation details that were fixed in all simulations and experiments. §VI.B studies estimator statistics in numerical simulations. §VI.C and §VI.D respectively compare PERK performance in phantom and *in vivo* experiments.

### A. Methods

In all simulations and experiments, we used data arising from a fast acquisition [14] consisting of two spoiled gradient-recalled echo (SPGR) [41] and one dual-echo steady-state (DESS) [42] scans. Since each SPGR (DESS) scan generates one (two) signal(s) per excitation, this acquisition yielded  $D \leftarrow 4$  datasets. We fixed scan parameters to be identical to those in [14], wherein repetition times and flip angles were optimized for precise  $T_1$  and  $T_2$  estimation in cerebral tissue at 3T field strength [14] and echo times were fixed across scans. We used standard magnitude<sup>3</sup> SPGR and DESS signal models expressed as a function of four free parameters per voxel: flip angle spatial variation (due to transmit field inhomogeneity)  $\kappa$ ; longitudinal and transverse relaxation time constants  $T_1$  and  $T_2$ ; and a pure-real proportionality constant  $M_0$ . We assumed prior knowledge of  $K \leftarrow 1$  known parameter  $\nu \leftarrow \kappa$  (in

<sup>3</sup>Standard complex DESS signal models depend on a fifth free parameter associated with phase accrual due to off-resonance effects. Because the first and second DESS signals depend differently on off-resonance phase accrual [14], off-resonance related phase (unlike signal loss) cannot be collected into the (now complex) proportionality constant. To avoid (separate or joint) estimation of an off-resonance field map, we followed [14] and used magnitude SPGR and DESS signal models. We accounted for consequently Rician-distributed noise in magnitude image data during training.

experiments, through separate acquisition and estimation of flip angle scaling maps) and collected the remaining  $L \leftarrow 3$  latent parameters as  $\mathbf{x} \leftarrow [M_0, T_1, T_2]^\top$ .

We used the same PERK training and testing process across all simulations and experiments. We assumed a separable prior distribution  $\mathbf{p}_{\mathbf{x}, \nu} \leftarrow \mathbf{p}_{M_0, T_1, T_2, \kappa} \equiv \mathbf{p}_{M_0} \mathbf{p}_{T_1} \mathbf{p}_{T_2} \mathbf{p}_{\kappa}$  and estimated flip angle scaling marginal distribution  $\mathbf{p}_{\kappa}$  from known  $\kappa$  map voxels via kernel density estimation (implemented using the built-in MATLAB<sup>®</sup> function `fitdist` with default options). To match the scaling of training and test data, we set  $M_0$  marginal distribution  $\mathbf{p}_{M_0} \leftarrow \text{unif}(2.2 \times 10^{-16}, u)$ , with  $u$  set as  $6.67 \times$  the maximum value of magnitude test data. We chose the supports of  $T_1, T_2$  marginal distributions  $\mathbf{p}_{T_1} \leftarrow \text{logunif}(400, 2000)\text{ms}$ ,  $\mathbf{p}_{T_2} \leftarrow \text{logunif}(40, 200)\text{ms}$  and clipped the support of  $\mathbf{p}_{\kappa}$  to assign nonzero probability only within  $[0.5, 2]$  such that these supports coincided with the supports over which [14] optimized the acquisition. We assumed noise covariance  $\Sigma$  of form  $\sigma^2 \mathbf{I}_4$  (as in [14]) and estimated the noise variance  $\sigma^2$  from Rayleigh-distributed regions of magnitude test data, using estimators described in [43]. We sampled  $N \leftarrow 10^6$  latent and known parameter realizations from these distributions and evaluated SPGR and DESS signal models to generate corresponding noiseless measurements. After adding complex Gaussian noise realizations, we concatenated the (Rician) magnitude of these noisy measurements with known parameter realizations to construct pure-real regressors. We separately selected and then held fixed free parameters  $\lambda \leftarrow 2^{0.6}$  and  $\rho \leftarrow 2^{-41}$  via a simple holdout process in simulation, described in §S.I. We set Gaussian kernel bandwidth matrix  $\Lambda$  from test data via (25). We sampled  $\nu, s \in Z \leftarrow 10^3$  times to construct approximate feature map  $\tilde{\mathbf{z}}$ . For each latent parameter  $l \leftarrow \{1, \dots, L\}$ , we applied  $\tilde{\mathbf{z}}$  to training data; computed sample means  $m_{x_l}, \mathbf{m}_{\tilde{\mathbf{z}}}$  and sample covariances  $\mathbf{c}_{z x_l}, \mathbf{C}_{\tilde{\mathbf{z}}\tilde{\mathbf{z}}}$ ; and evaluated (23) on test image data and the known flip angle scaling map on a per-voxel basis.

We evaluated PERK latent parameter estimates against ML estimates achieved via the variable projection method (VPM) [44] and exhaustive grid search. Following [14], we clustered flip angle scaling map voxels into 20 clusters via  $k$ -means++ [45] and used each of the 20 cluster means along with 500  $T_1$  and  $T_2$  values logarithmically spaced between  $(10^{1.5}, 10^{3.5})$  and  $(10^{0.5}, 10^3)$  to compute 20 dictionaries, each consisting of 250,000 signal vectors (fewer clusters introduced noticeable errors in experiments). Iterating over clusters, we generated each cluster’s dictionary and applied VPM and grid search over magnitude image data voxels assigned to that cluster.

We performed all simulations and experiments running MATLAB<sup>®</sup> R2013a on a 3.5GHz desktop computer equipped with 32GB RAM. Because our experiments use a single slice of image data, we report PERK training and testing times separately and note that only the latter time would scale linearly with the number of voxels (the former would scale negligibly due only to online model selection). In the interest of reproducible research, code and data will be freely available at <https://gitlab.eecs.umich.edu/fessler/qmri>.

	Truth	VPM	PERK
WM $T_1$	832	831.9 ± 17.2 (17.2)	830.3 ± 16.2 (16.2)
GM $T_1$	1331	1331.2 ± 30.9 (30.9)	1337.3 ± 30.1 (30.7)
WM $T_2$	79.6	79.61 ± 0.982 (0.983)	79.87 ± 0.976 (1.014)
GM $T_2$	110.	109.99 ± 1.38 (1.38)	109.82 ± 1.37 (1.38)

TABLE I: Sample means ± sample standard deviations (RMSEs) of VPM and PERK  $T_1, T_2$  estimates, computed in simulation over 7810 WM-like and 9162 GM-like voxels. Each sample statistic is rounded off to the highest place value of its (unreported) standard error, computed via formulas in [48]. All values are reported in milliseconds.

### B. Numerical Simulations

We assigned typical  $T_1, T_2$  values in white matter (WM) and grey matter (GM) at 3T [46] to the discrete anatomy of the 81st slice of the BrainWeb digital phantom [47] to produce ground truth  $M_0, T_1, T_2$  maps. We simulated  $217 \times 181$  noiseless single-coil SPGR and DESS image data, modeling (and then assuming as known) 20% flip angle spatial variation  $\kappa$ . We corrupted noiseless datasets with additive complex Gaussian noise to yield noisy complex datasets with SNR ranging from 94-154 in WM and 82-154 in GM, where SNR is defined

$$\text{SNR}(\tilde{\mathbf{y}}, \tilde{\boldsymbol{\epsilon}}) := \|\tilde{\mathbf{y}}\|_2 / \|\tilde{\boldsymbol{\epsilon}}\|_2 \quad (26)$$

for image data voxels  $\tilde{\mathbf{y}}$  and noise voxels  $\tilde{\boldsymbol{\epsilon}}$  within a region of interest (ROI) of a single SPGR/DESS dataset. We estimated  $M_0, T_1, T_2$  voxel-by-voxel from noisy magnitude images and known  $\kappa$  maps using PERK and VPM. PERK training and testing respectively took 32.1s and 1.5s, while VPM took 781s.

Table I compares sample statistics of PERK and VPM  $T_1, T_2$  estimates, computed over 7810 WM-like and 9162 GM-like voxels (§S.II presents corresponding images and  $M_0$  sample statistics). Overall, PERK and VPM both achieve excellent performance. PERK estimates are slightly more precise but slightly less accurate than VPM estimates. PERK root mean squared errors (RMSEs) are comparable to VPM RMSEs.

### C. Phantom Experiments

Phantom experiments used datasets from fast coronal scans of a High Precision Devices<sup>®</sup> MR system phantom  $T_2$  array acquired on a 3T GE Discovery<sup>™</sup> scanner with an 8-channel receive head array. This acquisition consisted of: two SPGR scans with 5, 15° flip angles and 12.2, 12.2ms repetition times; one DESS scan with 30° flip angle and 17.5ms repetition time; and two Bloch-Siebert (BS) scans [21] (for separate flip angle scaling  $\kappa$  estimation). Nominal flip angles were achieved by scaling a 2cm slab-selective Shinnar-Le Roux RF excitation [49] of duration 1.28ms and time-bandwidth product 4. All scans collected fully-sampled 3D Cartesian data using 4.67ms echo times with a  $256 \times 256 \times 8$  matrix over a  $24 \times 24 \times 4\text{cm}^3$  field of view. Scan time totaled 3m17s. Further acquisition details are reported in [14].

For each SPGR, DESS, and BS dataset, we reconstructed raw coil images via 3D Fourier transform and subsequently processed only one image slice centered within the excitation slab. We combined SPGR and DESS coil images using a natural extension of [50] to the case of multiple datasets.

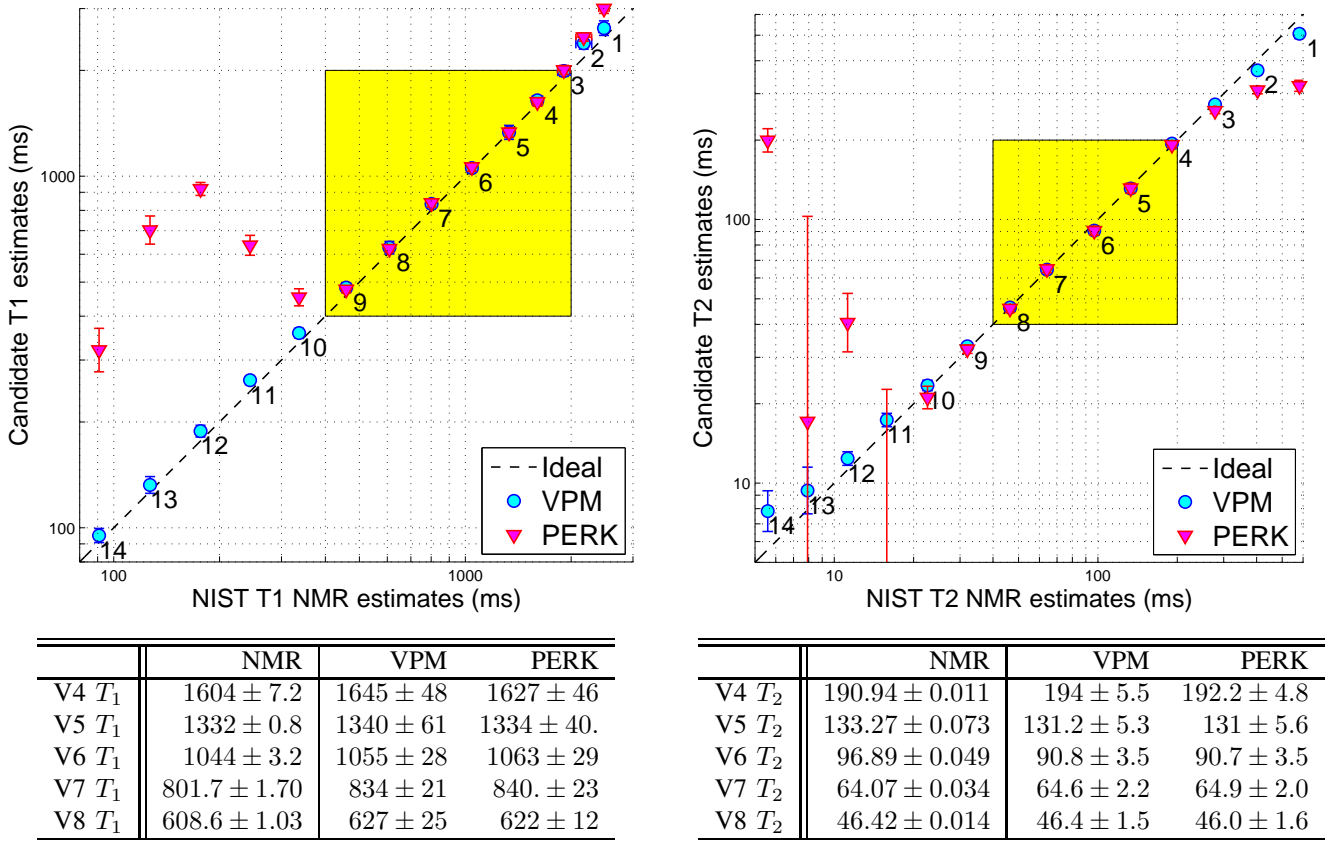


Fig. 1: Phantom sample statistics of VPM and PERK  $T_1, T_2$  estimates and NIST NMR reference measurements [40]. Plot markers and error bars indicate sample means and sample standard deviations computed over ROIs within the 14 vials labeled and color-coded in Fig. S.5. Yellow box boundaries indicate projections of the PERK sampling distribution’s support  $\text{supp}(p_{x,\nu})$ . Missing markers lie outside axis limits. Corresponding tables replicate sample means  $\pm$  sample standard deviations for vials within  $\text{supp}(p_{x,\nu})$ . Each value is rounded off to the highest place value of its (unreported) standard error, computed via formulas in [48]. ‘V#’ indicates vial numbers. All values are reported in milliseconds. Within  $\text{supp}(p_{x,\nu})$ , VPM and PERK estimates agree excellently with each other and reasonably with NMR measurements.

We similarly (but separately) combined BS coil images and estimated  $\kappa$  maps by normalizing and calibrating regularized transmit field estimates [51] from complex coil-combined BS images. We estimated  $M_0, T_1, T_2$  voxel-by-voxel from magnitude SPGR/DESS images and  $\kappa$  maps using PERK and VPM. PERK training and testing respectively took 32.2s and 1.9s while VPM took 935s.

Fig. 1 compares sample means and sample standard deviations computed within ROIs of PERK and VPM  $T_1, T_2$  estimates (at 293K) against nuclear magnetic resonance (NMR) reference measurements from the National Institute for Standards of Technology (NIST) [40] (at 293.00K). Yellow box boundaries indicate projections of the PERK sampling distribution’s support  $\text{supp}(p_{x,\nu})$ . ROI labels correspond with vial markers depicted in images presented in §S.III.A. Within  $\text{supp}(p_{x,\nu})$ , corresponding tables demonstrate that PERK and VPM estimates agree well with each other and reasonably with NMR measurements. We do not expect good PERK performance outside  $\text{supp}(p_{x,\nu})$  and indeed observe poor ability to extrapolate. As discussed in §V.B.1 and demonstrated in §S.III.B, expanding  $\text{supp}(p_{x,\nu})$  well beyond the acquisition

design parameter range of interest can substantially reduce PERK performance for typical  $T_1, T_2$  WM and GM values.

#### D. In vivo Experiments

*In vivo* experiments used datasets from axial scans of a healthy volunteer acquired with a 32-channel Nova Medical® receive head array. To address bulk motion between scans, we rigidly registered coil-combined images to a reference before parameter estimation. All other data acquisition, image reconstruction, and parameter estimation details are the same as in phantom experiments (acquisition and reconstruction details are reported in [14]). PERK training and testing respectively took 32.3s and 1.6s while VPM took 837s.

Fig. 2 compares PERK and VPM  $M_0, T_1, T_2$  parameter estimates. The PERK  $M_0$  estimate appears smoothed (although no spatial regularization was used) but is otherwise very similar compared to the VPM  $M_0$  estimate. Narrow display ranges emphasize that PERK and VPM  $T_1, T_2$  estimates discern cortical WM/GM boundaries similarly, though PERK  $T_1$  WM estimates are noticeably higher. PERK and VPM  $T_2$  estimates are nearly indistinguishable in lateral regions but disagree

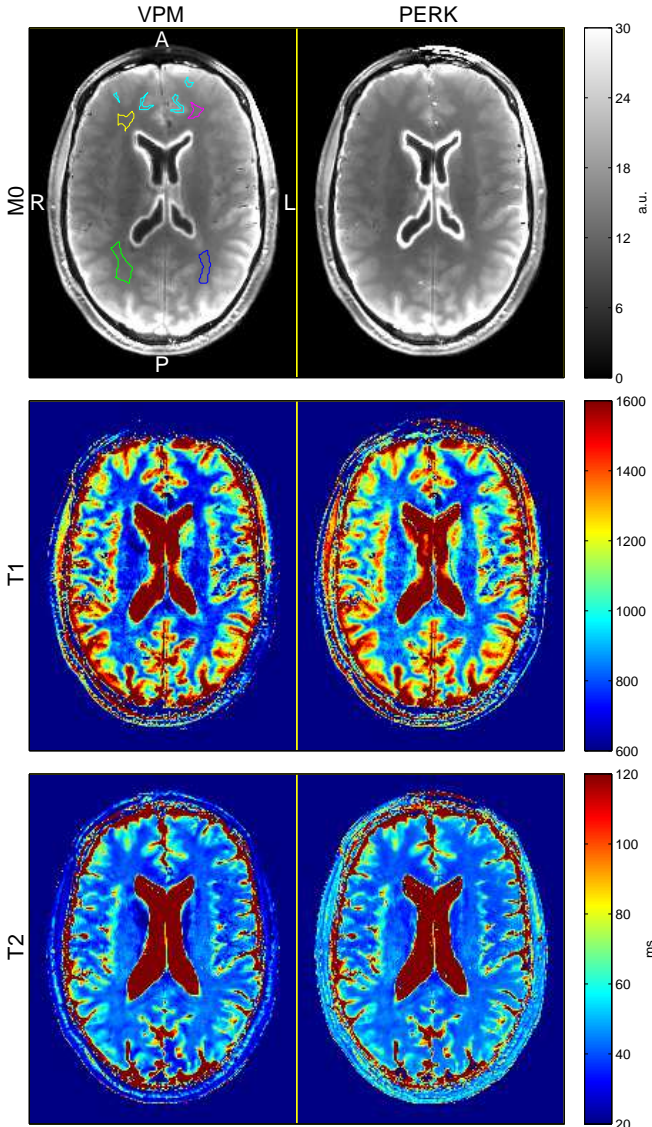


Fig. 2: VPM and PERK estimates of  $M_0, T_1, T_2$  in the brain of a healthy volunteer. Separate WM ROIs are distinguished by anterior/posterior (A/P) and right/left (R/L) directions. Four small anterior cortical GM polygons are pooled into a single GM ROI. Images are cropped in post-processing for display.

somewhat in medial regions close to cerebrospinal fluid (CSF). We neither expect nor observe reasonable PERK performance in voxels containing CSF.

Table II summarizes sample statistics of PERK and VPM  $T_1, T_2$  estimates, computed over four separate WM ROIs containing 96, 69, 224, and 148 voxels and one pooled cortical anterior GM ROI containing 156 voxels. Overall, PERK and VPM  $T_1, T_2$  ROI estimates are comparable.  $T_1$  estimates in GM and  $T_2$  estimates in WM/GM do not differ significantly. PERK  $T_1$  estimates are significantly higher than VPM  $T_1$  estimates in some WM ROIs; however, PERK  $T_1$  estimates are in closer agreement to literature measurements [46].

	ROI	VPM	PERK
$T_1$	AR WM	$778 \pm 28$	$842 \pm 30.$
	AL WM	$731 \pm 37$	$744 \pm 40.$
	PR WM	$805 \pm 52$	$838 \pm 48$
	PL WM	$789 \pm 40$	$825 \pm 40.$
	A GM	$1120 \pm 180$	$1150 \pm 164$
$T_2$	AR WM	$40.0 \pm 1.29$	$40.2 \pm 1.09$
	AL WM	$39.7 \pm 1.7$	$40.4 \pm 1.3$
	PR WM	$43.0 \pm 2.7$	$43.4 \pm 2.7$
	PL WM	$43.0 \pm 1.8$	$43.0 \pm 1.47$
	A GM	$53.5 \pm 11.8$	$53.2 \pm 11.8$

TABLE II: *In vivo* sample means  $\pm$  sample standard deviations of VPM and PERK  $T_1, T_2$  estimates, computed over color-coded ROIs indicated in Fig. 2. Each value is rounded off to the highest place value of its (unreported) standard error, computed via formulas in [48]. All values are in milliseconds.

## VII. DISCUSSION

The single-slice experiments demonstrate that PERK can achieve similar WM/GM  $T_1, T_2$  estimation performance as dictionary-based grid search via VPM, but in 1-2 orders of magnitude less time. This acceleration factor would grow to 2-3 orders of magnitude for  $T_1, T_2$  estimation over a typical full imaging volume (because PERK training time scales negligibly with the number of voxels) and to even higher orders of magnitude for full-volume parameter estimation in problems involving more latent parameters per voxel. Even with recent low-rank dictionary approximations [9], [12], [15], [16], dictionary-based methods are unlikely to achieve the large-scale speed of PERK.

PERK also handles known parameters  $\nu$  more naturally than does dictionary-based grid search. Grid search necessitates pre-clustering  $\nu$  voxel values and generating one dictionary per cluster; however, it is in general unclear *a priori* how many clusters are needed to balance accuracy and computation. In contrast, PERK simply considers the coordinates of each  $\nu$  sample as additional regressor dimensions. As the Gaussian PERK estimator is continuous in  $\nu$  (and  $\alpha$ ), Gaussian PERK does not suffer from either cluster (or grid) quantization bias.

Interestingly, PERK storage requirements grow more directly with regressor dimension  $P$  than with regressand dimension  $L$ . Using formulas for rank-one covariance matrix updates, constructing  $\hat{\mathbf{x}}(\cdot)$  element-wise via  $L$  evaluations of (23) can be implemented to use  $O(Z^2)$  memory units when  $\rho_l \leftarrow \rho \forall l \in \{1, \dots, L\}$  (as recommended in §V.B.2). Direct application of [35, Proposition 4] to the case of Gaussian kernel (12) reveals that  $Z$  should be scaled subquadratically but superlinearly with  $P$  to conservatively maintain a given threshold of maximal kernel approximation error. Thus, PERK memory requirements need grow no faster than  $O(P^4)$  to maintain a given level of kernel approximation error.

The  $O(P^4)$  PERK memory requirement ensures improvement over large-scale grid search in modestly overdetermined estimation problems, *i.e.* when  $P \approx L$ . In applications where the number of measurements far exceeds  $L$  (*e.g.*, MR fingerprinting [8]), PERK may still provide performance gains if images are projected [9] or directly reconstructed [15] into a low-dimensional measurement subspace prior to per-voxel



processing. Using this idea, we recently applied PERK to MR fingerprinting in [52].

Phantom experiments most clearly demonstrate that while PERK  $T_1, T_2$  estimates are accurate within a properly selected training range, PERK may extrapolate poorly outside the sampling distribution’s support (an improperly selected support can significantly degrade performance; see §S.III.B for a demonstration). If more graceful degradation is desired, it may be helpful to additionally fit coefficients of a low-order polynomial and thereby form estimates of form, e.g.,  $\hat{x}_l(\mathbf{p}) := \hat{h}_l(\mathbf{p}) + \hat{b}_l + \hat{\mathbf{c}}_l^T \mathbf{p}$ . However, greater model complexity may require more training samples to prevent overfitting.

The present formulation constructs separate scalar estimators for each coordinate of  $\hat{\mathbf{x}}$ . A natural extension might instead seek to construct vector estimators that consist of linear combinations of vector features that reside in an RKHS of vector-valued functions (see [53] for a review). Here, the associated reproducing kernel would now be matrix-valued and might encode expected dependencies among the outputs of  $\hat{\mathbf{x}}$ . With enough training points, the resulting vector estimator could achieve improved estimator performance in terms of accuracy and precision, at the expense of tuning more model parameters and increased computational burden.

Because there is ambiguity in MR data scale due to receive gains and other amplitude scaling factors, it is desirable to construct an estimator that is unaffected by changes in measurement scale between training and testing. In experiments, we address scaling ambiguity by setting the marginal  $M_0$  sampling distribution  $p_{M_0}$  based on test measurements, thereby matching simulated training measurement scale to test measurement scale. This strategy would require retraining between acquisitions that are different in scale but are otherwise identical, which may be undesirable in practice. As an alternative, one could preprocess each noisy training regressor and each noisy test measurement by rescaling each such that (without loss of generality) its first entry is unity, is subsequently uninformative, and can thus be safely pruned to reduce problem dimensionality. Training and testing estimators (for latent parameters other than  $M_0$ ) using these preprocessed regressors and test points is then largely invariant to the support of  $p_{M_0}$  [52]. One drawback to this approach is that normalization by noisy training regressors and test measurements could increase estimation variance.

As an alternative to PERK, researchers have recently proposed MRI parameter estimation via deep neural network learning [54], [55]. Deep learning requires enormous numbers of training points to train many model parameters without overfitting, and its limited theoretical basis renders its practical use largely an art. Here, we have introduced and investigated PERK with an emphasis on its simplicity and its relatively intuitive model selection (see §V.B); a thorough comparison with deep learning is a possible topic for future work.

## VIII. CONCLUSION

This paper has introduced PERK, a fast and general method for dictionary-free MRI parameter estimation. PERK first uses prior parameter/noise distributions and a general nonlinear

MR signal model to simulate many parameter-measurement training points and then constructs a nonlinear regression function from these training points using linear combinations of nonlinear kernels. We have demonstrated PERK for  $T_1, T_2$  estimation from optimized SPGR/DESS acquisitions [14], a simple application where it is straightforward to validate PERK estimates against gold-standard VPM estimates and NIST measurements. Numerical simulations showed that PERK achieves  $T_1, T_2$  RMSE comparable to VPM in WM- and GM-like voxels. Phantom experiments showed that within a properly chosen sampling distribution support, PERK and VPM estimates agree excellently with each other and reasonably with NIST NMR measurements. *In vivo* experiments showed that PERK and VPM produce comparable  $T_1$  estimates and nearly indistinguishable  $T_2$  estimates in WM and GM ROIs. PERK used identical model selection parameters across all simulations and experiments and consistently provided at least a  $23\times$  acceleration over VPM. This acceleration factor will increase by several orders of magnitude for estimation problems involving more latent parameters per voxel [22].

## ACKNOWLEDGMENTS

We thank Dr. Kathryn Keenan and Dr. Stephen Russek at NIST for generously lending a prototype [56] (used during acquisition testing) of the High Precision Devices® phantom.

## REFERENCES

- [1] F. Bloch, “Nuclear induction,” *Phys. Rev.*, vol. 70, no. 7-8, pp. 460–74, Oct. 1946.
- [2] H. C. Torrey, “Bloch equations with diffusion terms,” *Phys. Rev.*, vol. 104, pp. 563–5, 1956.
- [3] H. M. McConnell, “Reaction rates by nuclear magnetic resonance,” *J. of Chemical Phys.*, vol. 28, no. 3, pp. 430–31, Mar. 1958.
- [4] N. Bloembergen, E. M. Purcell, and R. V. Pound, “Relaxation effects in nuclear magnetic resonance absorption,” *Phys. Rev.*, vol. 73, no. 7, pp. 679–712, Apr. 1948.
- [5] D. L. Bihan, J.-F. Mangin, C. Poupon, C. A. Clark, S. Pappata, N. Molko, and H. Chabriet, “Diffusion tensor imaging: Concepts and applications,” *J. Mag. Res. Im.*, vol. 13, no. 4, pp. 534–546, Apr. 2001.
- [6] A. Mackay, K. Whittall, J. Adler, D. Li, D. Paty, and D. Graeb, “In vivo visualization of myelin water in brain by magnetic resonance,” *Mag. Res. Med.*, vol. 31, no. 6, pp. 673–7, Jun. 1994.
- [7] E. Staroswiecki, K. L. Granlund, M. T. Alley, G. E. Gold, and B. A. Hargreaves, “Simultaneous estimation of T2 and apparent diffusion coefficient in human articular cartilage in vivo with a modified three-dimensional double echo steady state (DESS) sequence at 3 T,” *Mag. Res. Med.*, vol. 67, no. 4, pp. 1086–96, 2012.
- [8] D. Ma, V. Gulani, N. Seiberlich, K. Liu, J. L. Sunshine, J. L. Duerk, and M. A. Griswold, “Magnetic resonance fingerprinting,” *Nature*, vol. 495, pp. 187–93, Mar. 2013.
- [9] D. F. McGivney, E. Pierre, D. Ma, Y. Jiang, H. Saybasili, V. Gulani, and M. A. Griswold, “SVD compression for magnetic resonance fingerprinting in the time domain,” *IEEE Trans. Med. Imag.*, vol. 33, no. 12, pp. 2311–22, Dec. 2014.
- [10] B. Zhao, F. Lam, and Z.-P. Liang, “Model-based MR parameter mapping with sparsity constraints: parameter estimation and performance bounds,” *IEEE Trans. Med. Imag.*, vol. 33, no. 9, pp. 1832–44, Sep. 2014.
- [11] N. Ben-Eliezer, D. K. Sodickson, and K. T. Block, “Rapid and accurate T2 mapping from multi-spin-echo data using Bloch-simulation-based reconstruction,” *Mag. Res. Med.*, vol. 73, no. 2, pp. 809–17, Feb. 2015.
- [12] S. F. Cauley, K. Setsompop, D. Ma, Y. Jiang, H. Ye, E. Adalsteinsson, M. A. Griswold, and L. L. Wald, “Fast group matching for MR fingerprinting reconstruction,” *Mag. Res. Med.*, vol. 74, no. 2, pp. 523–8, Aug. 2015.
- [13] B. Zhao, K. Setsompop, H. Ye, S. Cauley, and L. L. Wald, “Maximum likelihood reconstruction for magnetic resonance fingerprinting,” *IEEE Trans. Med. Imag.*, vol. 35, no. 8, pp. 1812–23, Aug. 2016.

- [14] G. Nataraj, J.-F. Nielsen, and J. A. Fessler, "Optimizing MR scan design for model-based T1, T2 estimation from steady-state sequences," *IEEE Trans. Med. Imag.*, vol. 36, no. 2, pp. 467–77, Feb. 2017.
- [15] J. Assländer, M. A. Cloos, F. Knoll, D. K. Sodickson, Jürgen. Hennig, and R. Lattanzi, "Low rank alternating direction method of multipliers reconstruction for MR fingerprinting," *Mag. Res. Med.*, 2017.
- [16] M. Yang, D. Ma, Y. Jiang, J. Hamilton, N. Seiberlich, M. A. Griswold, and D. McGivney, "Low rank approximation methods for MR fingerprinting with large scale dictionaries," *Mag. Res. Med.*, 2017.
- [17] D. A. Feinberg, L. E. Crooks, P. Sheldon, J. H. Iii, J. Watts, and M. Arakawa, "Magnetic resonance imaging the velocity vector components of fluid flow," *Mag. Res. Med.*, vol. 2, no. 6, pp. 555–66, Dec. 1985.
- [18] D. S. Tuch, V. J. Wedeen, A. M. Dale, J. S. George, and J. W. Belliveau, "Conductivity tensor mapping of the human brain using diffusion tensor MRI," *Proc. Natl. Acad. Sci.*, vol. 98, no. 20, pp. 11 697–701, Sep. 2001.
- [19] K. Sekihara, S. Matsui, and H. Kohno, "NMR imaging for magnets with large nonuniformities," *IEEE Trans. Med. Imag.*, vol. 4, no. 4, pp. 193–9, Dec. 1985.
- [20] G. R. Morrell, "A phase-sensitive method of flip angle mapping," *Mag. Res. Med.*, vol. 60, no. 4, pp. 889–94, Oct. 2008.
- [21] L. I. Sacolick, F. Wiesinger, I. Hancu, and M. W. Vogel, "B1 mapping by Bloch-Siegert shift," *Mag. Res. Med.*, vol. 63, no. 5, pp. 1315–22, May 2010.
- [22] G. Nataraj, J.-F. Nielsen, and J. A. Fessler, "Myelin water fraction estimation from optimized steady-state sequences using kernel ridge regression," in *Proc. Intl. Soc. Mag. Res. Med.*, 2017, p. 5076.
- [23] S. C. L. Deoni, B. K. Rutt, T. Arun, C. Pierpaoli, and D. K. Jones, "Gleaning multicomponent T1 and T2 information from steady-state imaging data," *Mag. Res. Med.*, vol. 60, no. 6, pp. 1372–87, Dec. 2008.
- [24] S. C. L. Deoni, L. Matthews, and S. H. Kolind, "One component? Two components? Three? The effect of including a nonexchanging "free" water component in multicomponent driven equilibrium single pulse observation of T1 and T2," *Mag. Res. Med.*, vol. 70, no. 1, pp. 147–54, Jul. 2013.
- [25] G. S. Kimeldorf and G. A. Wahba, "A correspondence between Bayesian estimation on stochastic processes and smoothing by splines," *Ann. Math. Stat.*, vol. 41, no. 2, pp. 495–502, Apr. 1970.
- [26] N. Aronszajn, "Theory of reproducing kernels," *Trans. Amer. Math. Soc.*, vol. 68, no. 3, pp. 337–404, May 1950. [Online]. Available: <http://www.jstor.org/stable/1990404>
- [27] C. Cortes and V. Vapnik, "Support-vector networks," *Mach. Learn.*, vol. 20, no. 3, pp. 273–97, Sep. 1995.
- [28] C. Saunders, A. Gammerman, and V. Vovk, "Ridge regression learning algorithm in dual variables," in *Proc. Intl. Conf. Mach. Learn.*, 1998, pp. 515–21.
- [29] G. Nataraj, J.-F. Nielsen, and J. A. Fessler, "Dictionary-free MRI parameter estimation via kernel ridge regression," in *Proc. IEEE Intl. Symp. Biomed. Imag.*, 2017, pp. 5–9.
- [30] B. Schölkopf, R. Herbrich, and A. J. Smola, "A generalized representer theorem," in *Proc. Computational Learning Theory (COLT)*, 2001, pp. 416–426, INCS 2111.
- [31] A. E. Hoerl and R. W. Kennard, "Ridge regression: biased estimation for nonorthogonal problems," *Technometrics*, vol. 12, no. 1, pp. 55–67, Feb. 1970. [Online]. Available: <http://www.jstor.org/stable/1267351>
- [32] I. Steinwart and A. Christmann, *Support vector machines*. Springer, 2008.
- [33] H. Gudbjartsson and S. Patz, "The Rician distribution of noisy MRI data," *Mag. Res. Med.*, vol. 34, no. 6, pp. 910–4, Dec. 1995.
- [34] A. Rahimi and B. Recht, "Random features for large-scale kernel machines," in *NIPS*, 2007. [Online]. Available: <https://papers.nips.cc/paper/3182-random-features-for-large-scale-kernel-machines>
- [35] D. J. Sutherland and J. Schneider, "On the error of random Fourier features," in *Proc. Intl. Conf. on Uncertainty in AI*, 2015. [Online]. Available: <http://arxiv.org/abs/1506.02785>
- [36] Z. Wu, "Generalized Bochner's theorem for radial function," *Approximation Theory and its Applications*, vol. 13, no. 3, pp. 47–57, 1997.
- [37] M. A. Woodbury, "Inverting modified matrices," 1950, tech. Report 42, Stat. Res. Group, Princeton Univ.
- [38] V. N. Vapnik, *Statistical learning theory*. Wiley-Interscience, 1998.
- [39] H. Cramér, *Mathematical methods of statistics*. Princeton: Princeton Univ. Press, 1946. [Online]. Available: <http://press.princeton.edu/titles/391.html>
- [40] K. E. Keenan, K. F. Stupic, M. A. Boss, S. E. Russek, T. L. Chenevert, P. V. Prasad, W. E. Reddick, K. M. Cecil, J. Zheng, P. Hu, and E. F. Jackson, "Multi-site, multi-vendor comparison of T1 measurement using ISMRM/NIST system phantom," in *Proc. Intl. Soc. Mag. Res. Med.*, 2016, p. 3290.
- [41] Y. Zur, M. L. Wood, and L. J. Neuringer, "Spoiling of transverse magnetization in steady-state sequences," *Mag. Res. Med.*, vol. 21, no. 2, pp. 251–63, Oct. 1991.
- [42] H. Bruder, H. Fischer, R. Graumann, and M. Deimling, "A new steady-state imaging sequence for simultaneous acquisition of two MR images with clearly different contrasts," *Mag. Res. Med.*, vol. 7, no. 1, pp. 35–42, May 1988.
- [43] M. M. Siddiqui, "Statistical inference for Rayleigh distributions," *RADIO SCIENCE Journal of Research NBS/USNC-URSI*, vol. 68D, no. 9, pp. 1005–10, Sep. 1964. [Online]. Available: [http://nvlpubs.nist.gov/nistpubs/jres/68D/jresv68Dn9p1005\\_A1b.pdf](http://nvlpubs.nist.gov/nistpubs/jres/68D/jresv68Dn9p1005_A1b.pdf)
- [44] G. Golub and V. Pereyra, "Separable nonlinear least squares: the variable projection method and its applications," *Inverse Prob.*, vol. 19, no. 2, pp. R1–26, Apr. 2003.
- [45] D. Arthur and S. Vassilvitskii, "K-means++: The advantages of careful seeding," in *Proc. 18th Annual ACM-SIAM Symp. Disc. Alg. (SODA)*, 2007, pp. 1027–35. [Online]. Available: <http://dl.acm.org/citation.cfm?id=1283494>
- [46] J. P. Wansapura, S. K. Holland, R. S. Dunn, and W. S. Ball, "NMR relaxation times in the human brain at 3.0 Tesla," *J. Mag. Res.*, vol. 9, no. 4, pp. 531–8, Apr. 1999.
- [47] D. L. Collins, A. P. Zijdenbos, V. Kollokian, J. G. Sled, N. J. Kabani, C. J. Holmes, and A. C. Evans, "Design and construction of a realistic digital brain phantom," *IEEE Trans. Med. Imag.*, vol. 17, no. 3, pp. 463–8, Jun. 1998.
- [48] S. Ahn and J. A. Fessler, "Standard errors of mean, variance, and standard deviation estimators," *Comm. and Sign. Proc. Lab.*, Dept. of EECS, Univ. of Michigan, Ann Arbor, MI, 48109-2122, Tech. Rep. 413, Jul. 2003. [Online]. Available: <http://web.eecs.umich.edu/~fessler/papers/lists/files/tr/stderr.pdf>
- [49] J. Pauly, P. Le Roux, D. Nishimura, and A. Macovski, "Parameter relations for the Shinnar-Le Roux selective excitation pulse design algorithm," *IEEE Trans. Med. Imag.*, vol. 10, no. 1, pp. 53–65, Mar. 1991.
- [50] L. Ying and J. Sheng, "Joint image reconstruction and sensitivity estimation in SENSE (JSENSE)," *Mag. Res. Med.*, vol. 57, no. 6, pp. 1196–1202, Jun. 2007.
- [51] H. Sun, W. A. Grissom, and J. A. Fessler, "Regularized estimation of Bloch-Siegert B1+ Maps in MRI," in *Proc. IEEE Intl. Conf. on Image Processing*, 2014, pp. 3646–50.
- [52] G. Nataraj, M. Gao, J. Assländer, C. Scott, and J. A. Fessler, "Shallow learning with kernels for dictionary-free magnetic resonance fingerprinting," in *ISMRM Workshop on MR Fingerprinting*, 2017, to appear.
- [53] M. A. Alvarez, L. Rosasco, and N. D. Lawrence, "Kernels for vector-valued functions: A review," *MIT, CSAIL, Tech. Rep. MIT-CSAIL-TR-2011-033*, Jun. 2011. [Online]. Available: <http://cbcl.mit.edu/publications/ps/MIT-CSAIL-TR-2011-033.pdf>
- [54] O. Cohen, B. Zhu, and M. Rosen, "Deep learning for fast MR fingerprinting reconstruction," in *Proc. Intl. Soc. Mag. Res. Med.*, 2017, p. 0688.
- [55] P. Virtue, S. X. Yu, and M. Lustig, "Better than real: Complex-valued neural nets for MRI fingerprinting," in *Proc. IEEE Intl. Conf. on Image Processing*, 2017, to appear.
- [56] S. E. Russek, M. Boss, E. F. Jackson, D. L. Jennings, J. L. Evelhoch, J. L. Gunter, and A. G. Sorensen, "Characterization of NIST/ISMRM MRI system phantom," in *Proc. Intl. Soc. Mag. Res. Med.*, 2012, p. 2456. [Online]. Available: <http://cds.ismrm.org/protected/12MProceedings/files/2456.pdf>

# Supplementary Material for Dictionary-Free MRI PERK: Parameter Estimation via Regression with Kernels

Gopal Nataraj<sup>\*</sup>, Jon-Fredrik Nielsen<sup>†</sup>, Clayton Scott<sup>\*</sup>, and Jeffrey A. Fessler<sup>\*</sup>

This supplement elaborates upon methodology details and presents additional figures that could not be included in the manuscript due to page restrictions. §S.I details our procedure for selecting free model parameters. §S.II presents estimated parameter images corresponding to numerical simulations presented in §VI.B. §S.III provides additional phantom results and discusses PERK performance degradation when trained with latent parameter distributions that have wider support than the parameter ranges used for optimizing the scan design in [14].

## S.I. MODEL SELECTION VIA HOLDOUT

We selected Gaussian kernel bandwidth scaling parameter  $\lambda$  and regularization parameter  $\rho$  using the following simple holdout procedure in simulation. We discretized  $(\lambda, \rho)$  over a finely spaced grid spanning many orders of magnitude. Exactly as described in §VI.A, we trained a PERK estimator  $\hat{\mathbf{x}}_{\lambda, \rho}$  for each candidate model parameter setting. We tested each PERK estimator on a separate simulated dataset consisting of many samples from the training prior distribution  $\mathbf{p}_{\mathbf{x}, \nu}$ . We selected model parameters by exhaustively seeking a minimizer  $(\hat{\lambda}, \hat{\rho})$  of the ‘‘holdout’’ cost function

$$\Psi(\lambda, \rho) := \sqrt{\frac{1}{T} \sum_{t=1}^T \left\| [\text{diag}(\mathbf{x}_t)]^{-1} (\hat{\mathbf{x}}_{\lambda, \rho}(\mathbf{p}_t) - \mathbf{x}_t) \right\|_{\mathbf{W}}^2} \quad (\text{S.1})$$

where  $t \in \{1, \dots, T\}$  indexes  $T$  test points; each  $\mathbf{x}_t$  is the true latent parameter corresponding to holdout test data point  $\mathbf{p}_t$ ; and  $\mathbf{W}$  is a diagonal unit-trace weighting matrix. Intuitively,  $\Psi(\lambda, \rho)$  is the weighted normalized root mean squared error of PERK estimator  $\hat{\mathbf{x}}_{\lambda, \rho}$ , where the mean approximates an expectation with respect to  $\mathbf{p}_{\mathbf{x}, \nu}$  and the latent parameter weighting is specified by  $\mathbf{W}$ .

Fig. S.1 plots  $\Psi(\lambda, \rho)$  for  $T \leftarrow 10^5$  test points and  $\mathbf{W} \leftarrow \text{diag}([0, 0.5, 0.5]^T)$  selected to place equal emphasis on  $T_1, T_2$  estimation. We chose our fine grid search range using a preliminary coarse grid search spanning a much wider range of  $(\lambda, \rho)$  values. Overall, we observe a broad range of  $(\lambda, \rho)$  values that yield similar cost function values. Holdout cost  $\Psi(\lambda, \rho)$  gracefully increases with larger  $(\lambda, \rho)$  values due to under-fitting. For very small  $\rho$  values,  $\Psi(\lambda, \rho)$  can be large because poorly conditioned matrix inversions cause machine imprecision to dominate estimation error. In all simulations and experiments, we fixed free model parameters to the minimizer  $(\hat{\lambda}, \hat{\rho}) \leftarrow (2^{0.6}, 2^{-41})$ , indicated by a white star.

## S.II. NUMERICAL SIMULATIONS

	Truth	VPM	PERK
WM $M_0$	0.77	0.7699 $\pm$ 0.00919 (0.00920)	0.76936 $\pm$ 0.00870 (0.00873)
GM $M_0$	0.86	0.8601 $\pm$ 0.01186 (0.01186)	0.8614 $\pm$ 0.01141 (0.01149)
WM $T_1$	832	831.9 $\pm$ 17.2 (17.2)	830.3 $\pm$ 16.2 (16.2)
GM $T_1$	1331	1331.2 $\pm$ 30.9 (30.9)	1337.3 $\pm$ 30.1 (30.7)
WM $T_2$	79.6	79.61 $\pm$ 0.982 (0.983)	79.87 $\pm$ 0.976 (1.014)
GM $T_2$	110.	109.99 $\pm$ 1.38 (1.38)	109.82 $\pm$ 1.37 (1.38)

TABLE S.1: Sample means  $\pm$  sample standard deviations (RMSEs) of VPM and PERK  $M_0, T_1, T_2$  estimates, computed in simulation over 7810 WM-like and 9162 GM-like voxels. Each sample statistic is rounded off to the highest place value of its (unreported) standard error, computed via formulas in [48].  $M_0$  values are unitless.  $T_1, T_2$  values are reported in milliseconds and were also reported in Table I.

Figs. S.2, S.3, and S.4 respectively compare PERK and VPM  $M_0, T_1$ , and  $T_2$  estimates alongside  $10\times$  magnified absolute difference images with respect to the ground truth. Voxels not assigned WM- or GM-like relaxation times are masked out in post-processing for display. Table S.1 extends Table I to present  $M_0$  in addition to  $T_1, T_2$  sample statistics within WM- and GM-like ROIs. Difference images demonstrate that within WM- and GM-like voxels, PERK and VPM both exhibit low estimation error.

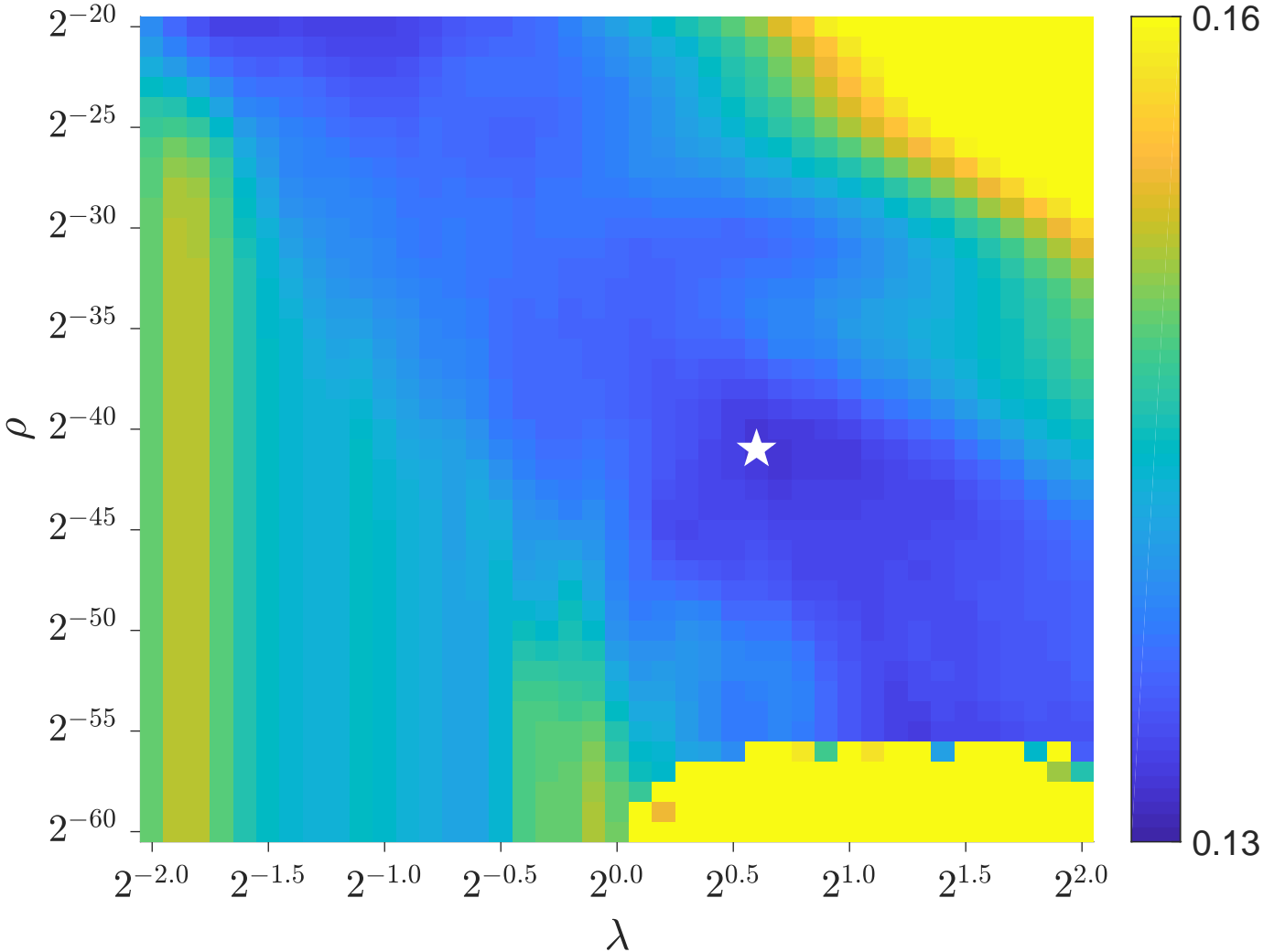


Fig. S.1: Holdout criterion  $\Psi(\lambda, \rho)$  versus Gaussian kernel bandwidth scaling parameter  $\lambda$  and regularization parameter  $\rho$ . Each pixel is the weighted normalized root mean squared error of a candidate PERK estimator, where the empirical mean over  $10^5$  test points approximates an expectation with respect to training prior distribution  $p_{\mathbf{x}, \nu}$  and the weighting places emphasis on good  $T_1, T_2$  estimation performance. A white star marks the minimizer  $(\hat{\lambda}, \hat{\rho}) \leftarrow (2^{0.6}, 2^{-41})$ .

### S.III. PHANTOM EXPERIMENTS

#### A. Training over a conservative sampling distribution support

Fig. S.5 compares PERK and VPM  $M_0, T_1, T_2$  estimates in a quantitative phantom. Vials are enumerated in descending  $T_1, T_2$  order. Vials whose  $T_1, T_2$  values are within sampling distribution support  $\text{supp}(p_{\mathbf{x}, \nu})$  (as measured by NIST NMR reference measurements [40]) have labels highlighted with yellow numbers. Here,  $\text{supp}(p_{\mathbf{x}, \nu})$  was chosen to reflect the ranges of latent parameter values for which the SPGR/DESS scan parameters were optimized in [14]. Circular ROIs are selected well away from vial encasings and correspond with sample statistics presented in Fig. 1. Distilled water surrounds the encased vials. Within the highlighted vials of interest, PERK and VPM estimates appear visually similar.

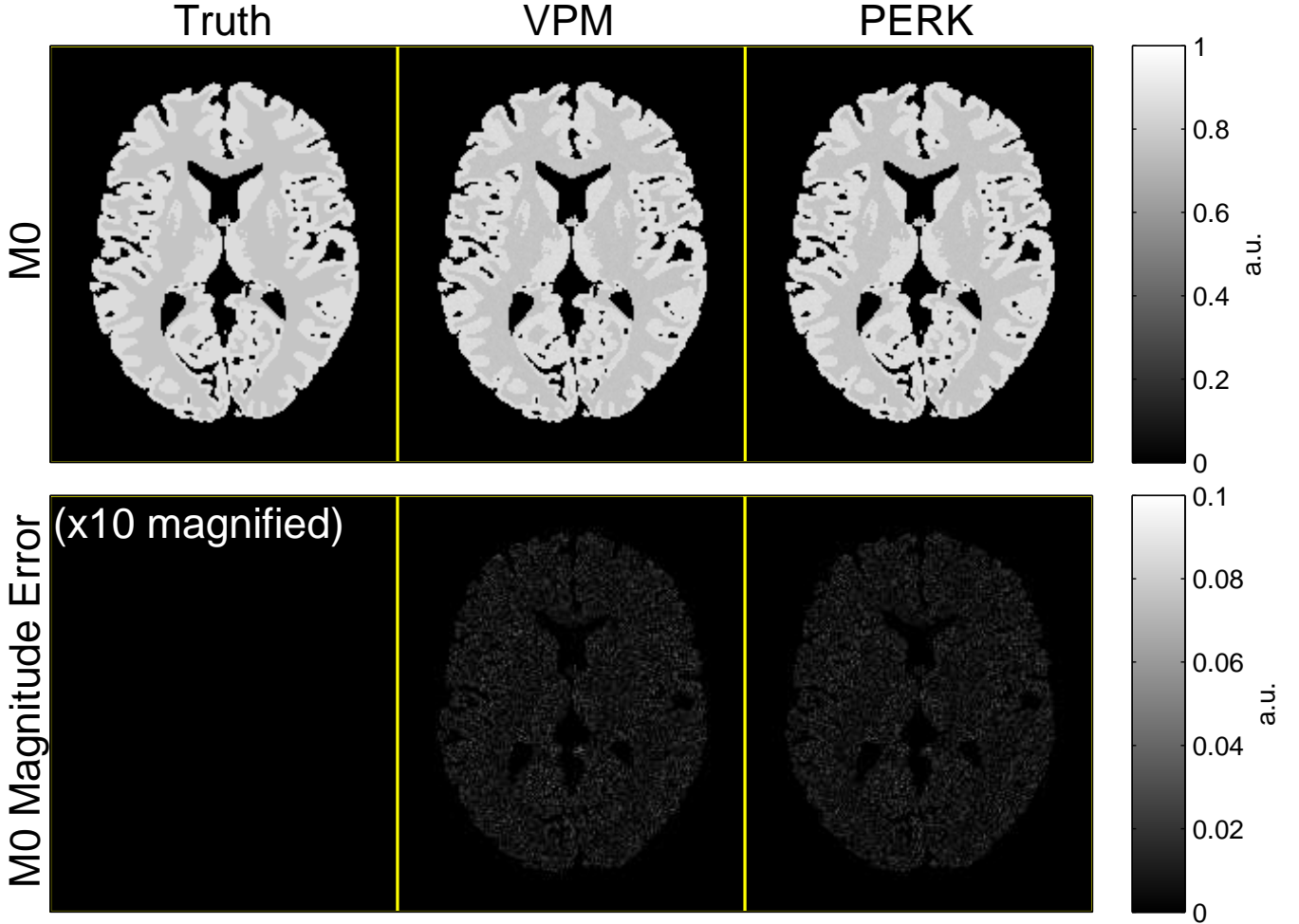


Fig. S.2:  $M_0$  VPM and PERK estimates and corresponding error images, in simulation. Magnitude error images are  $10\times$  magnified. Voxels not assigned WM- or GM-like relaxation times are masked out in post-processing for display. Difference images demonstrate that VPM and PERK  $M_0$  estimates both exhibit low estimation error. Table S.1 presents corresponding sample statistics.

### B. Training over an aggressive sampling distribution support

Although the SPGR/DESS acquisition was optimized in [14] for a certain range of  $T_1, T_2$  values, it is interesting to investigate how well PERK can perform outside that parameter range if presented (simulated) training data over a wider range of latent parameters. It is also interesting to explore whether using such a wider range of latent parameters for training degrades performance for the parameter range of primary interest. Thus, we repeated the phantom experiment described in §VI.C except now using a PERK estimator trained using a sampling prior distribution with broader support. We still assume a separable prior distribution  $p_{\mathbf{x}, \nu} \leftarrow p_{M_0} p_{T_1} p_{T_2} p_{\kappa}$  (with  $p_{M_0}$  and  $p_{\kappa}$  set as before) but now set  $p_{T_1} \leftarrow \text{logunif}(10^{1.5}, 10^{3.5})$  and  $p_{T_2} \leftarrow \text{logunif}(10^{0.5}, 10^{3.5})$  to have wider supports. These support endpoints now match the grid search support used by the VPM. All other training and testing details are unchanged from before.

Fig. S.6 is analogous to Fig. 1 in that it plots sample means and sample standard deviations computed within ROIs of PERK and VPM  $T_1, T_2$  estimates, except now using a PERK estimator trained over the broader sampling distribution. Fig. S.7 presents corresponding images. The yellow boxes are unchanged from Fig. 1 and so their boundaries no longer correspond to projections of the PERK sampling distribution's support. Rather, they serve to clearly highlight that PERK estimator performance can significantly deteriorate even over the parameter range of interest, when trained using a range of parameters that exceeds the design criteria of the acquisition.

Fig. S.6 also tabulates sample means and sample standard deviations computed within ROIs of vials 4-8. Comparing again with Fig. 1, PERK  $T_2$  estimation accuracy is more severely affected than  $T_1$  estimation accuracy (interestingly,  $T_1$  estimation accuracy is in fact improved for many vials). PERK  $T_1, T_2$  estimation precision is consistently worse in vials 4-8 when trained over the broader sampling range.

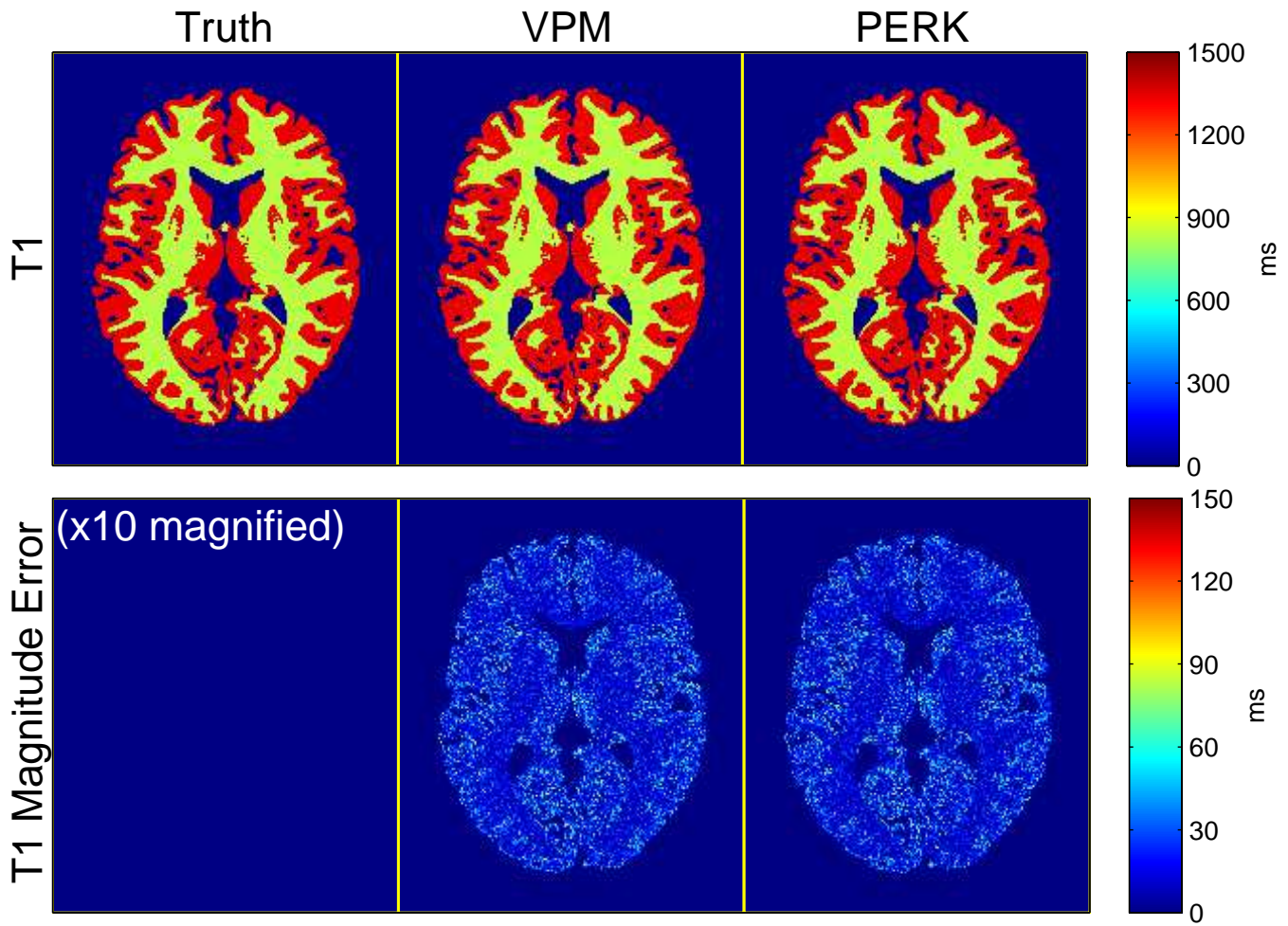


Fig. S.3:  $T_1$  VPM and PERK estimates and corresponding error images, in simulation. Magnitude error images are  $10\times$  magnified. Voxels not assigned WM- or GM-like relaxation times are masked out in post-processing for display. Difference images demonstrate that VPM and PERK  $T_1$  estimates both exhibit low estimation error. Tables I and S.1 both present the same corresponding sample statistics.

These observations highlight the importance of considering acquisition design and parameter estimation in tandem, and with consideration of the latent parameter ranges of interest in a given application.

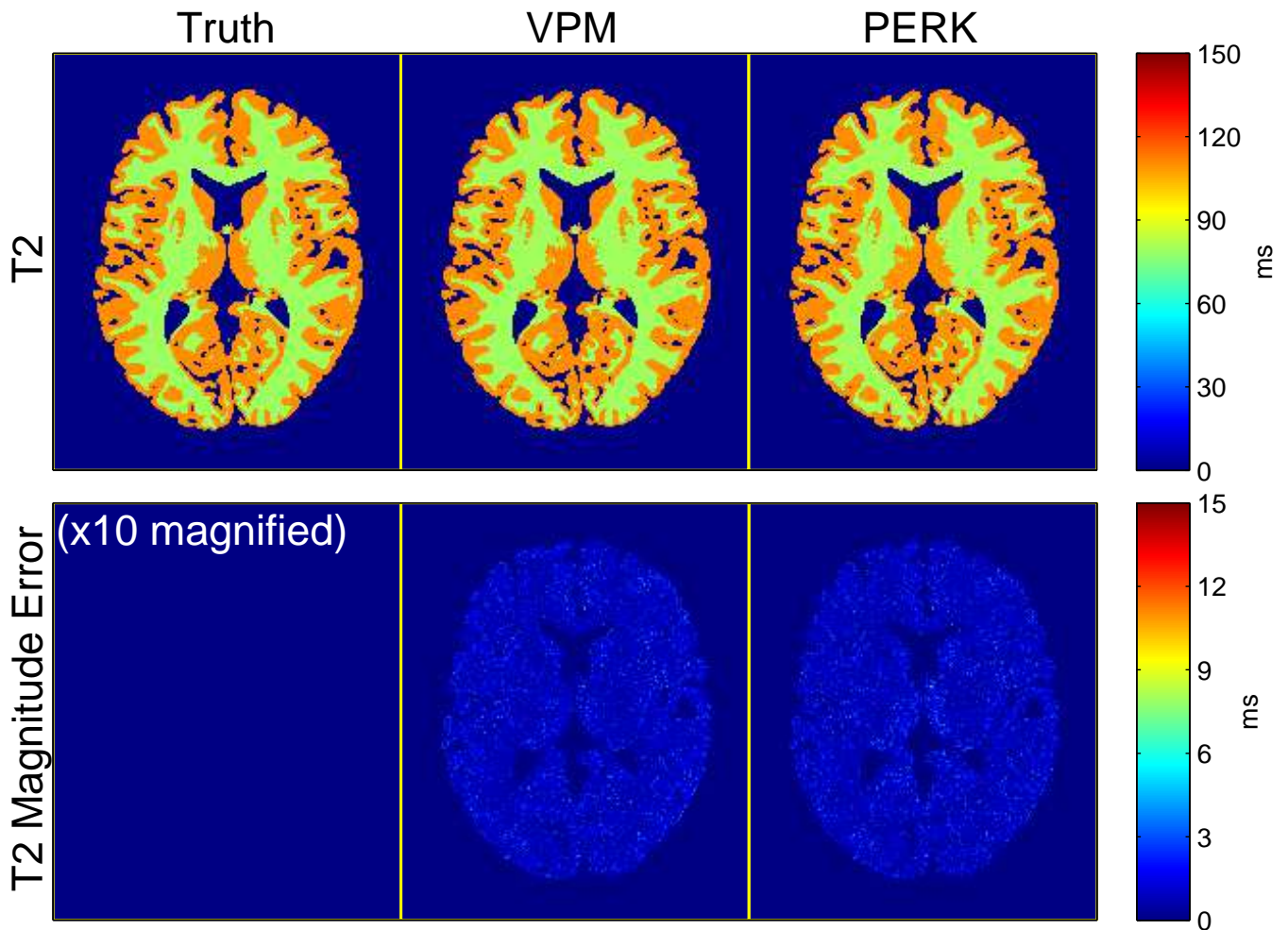


Fig. S.4:  $T_2$  VPM and PERK estimates and corresponding error images, in simulation. Magnitude error images are  $10\times$  magnified. Voxels not assigned WM- or GM-like relaxation times are masked out in post-processing for display. Difference images demonstrate that VPM and PERK  $T_2$  estimates both exhibit low estimation error. Tables I and S.1 both present the same corresponding sample statistics.

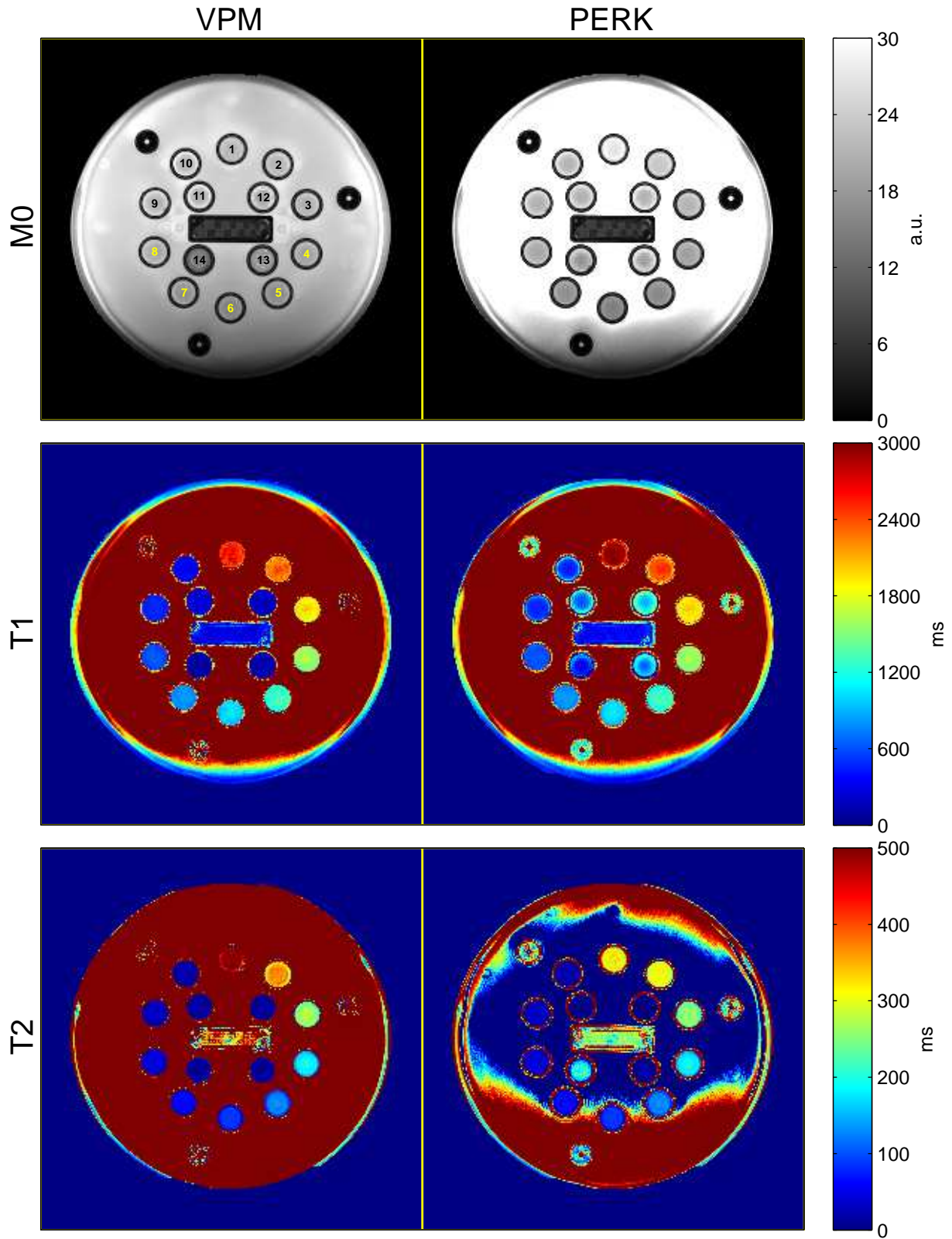
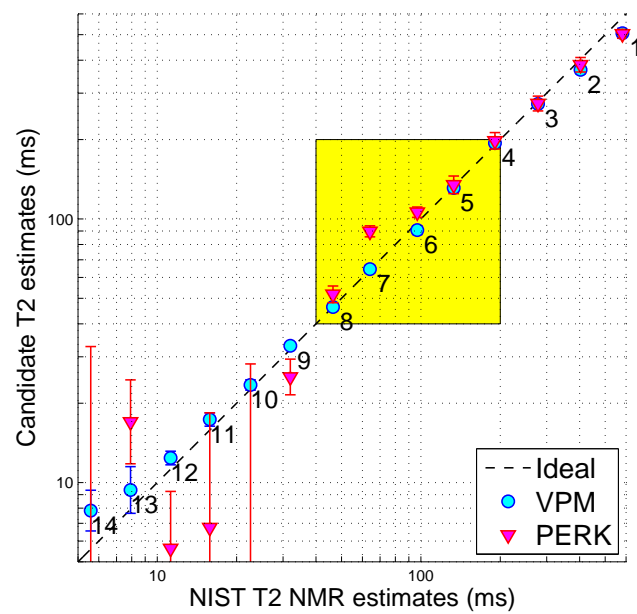
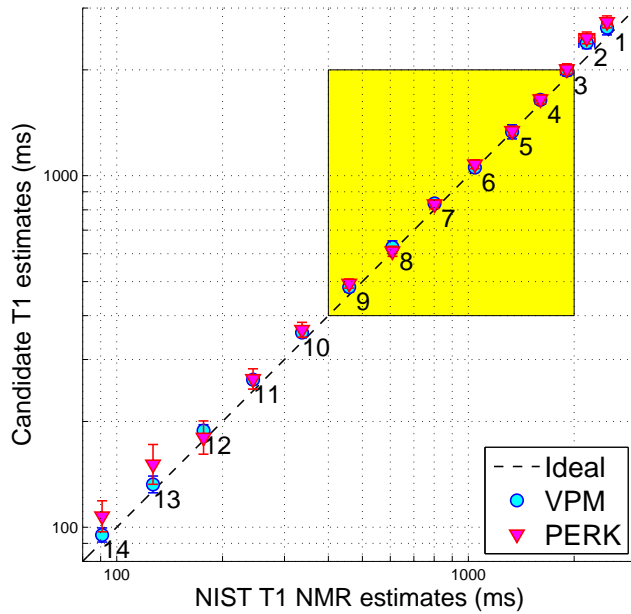


Fig. S.5: VPM and PERK  $M_0$ ,  $T_1$ ,  $T_2$  estimates in a quantitative phantom. Vials are enumerated and highlighted to correspond with markers and colored boxes in Fig. 1. PERK has only been trained to accurately estimate within vials 4-8; within these vials, VPM and PERK estimates appear visually similar.





	NMR	VPM	PERK
V4 $T_1$	$1604 \pm 7.2$	$1645 \pm 48$	$1651 \pm 51$
V5 $T_1$	$1332 \pm 0.8$	$1330 \pm 61$	$1342 \pm 40.$
V6 $T_1$	$1044 \pm 3.2$	$1055 \pm 28$	$1079 \pm 32$
V7 $T_1$	$801.7 \pm 1.70$	$834 \pm 21$	$830. \pm 24$
V8 $T_1$	$608.6 \pm 1.03$	$627 \pm 25$	$610. \pm 20.$

	NMR	VPM	PERK
V4 $T_2$	$190.94 \pm 0.011$	$194 \pm 5.5$	$198 \pm 15$
V5 $T_2$	$133.27 \pm 0.073$	$131.2 \pm 5.3$	$135 \pm 11$
V6 $T_2$	$96.89 \pm 0.049$	$90.8 \pm 3.5$	$106.2 \pm 4.9$
V7 $T_2$	$64.07 \pm 0.034$	$64.6 \pm 2.2$	$89.9 \pm 4.3$
V8 $T_2$	$46.42 \pm 0.014$	$46.4 \pm 1.5$	$51.9 \pm 3.8$

Fig. S.6: Phantom sample statistics of more aggressively trained VPM and PERK  $T_1, T_2$  estimates and NIST NMR reference measurements [40]. Unlike analogous results in Fig. 1, here the PERK estimator was trained with a sampling distribution whose support extended well beyond the range of  $T_1, T_2$  values for which the acquisition was optimized in [14]. Comparing to Fig. 1, we find that PERK estimator performance degrades within the highlighted  $T_1, T_2$  range of interest. Plot markers and error bars indicate sample means and sample standard deviations computed over ROIs within the 14 vials labeled and color-coded in Fig. S.7. Corresponding tables replicate sample means  $\pm$  sample standard deviations for vials within the highlighted range. Each value is rounded off to the highest place value of its (unreported) standard error, computed via formulas in [48]. All values are in milliseconds.

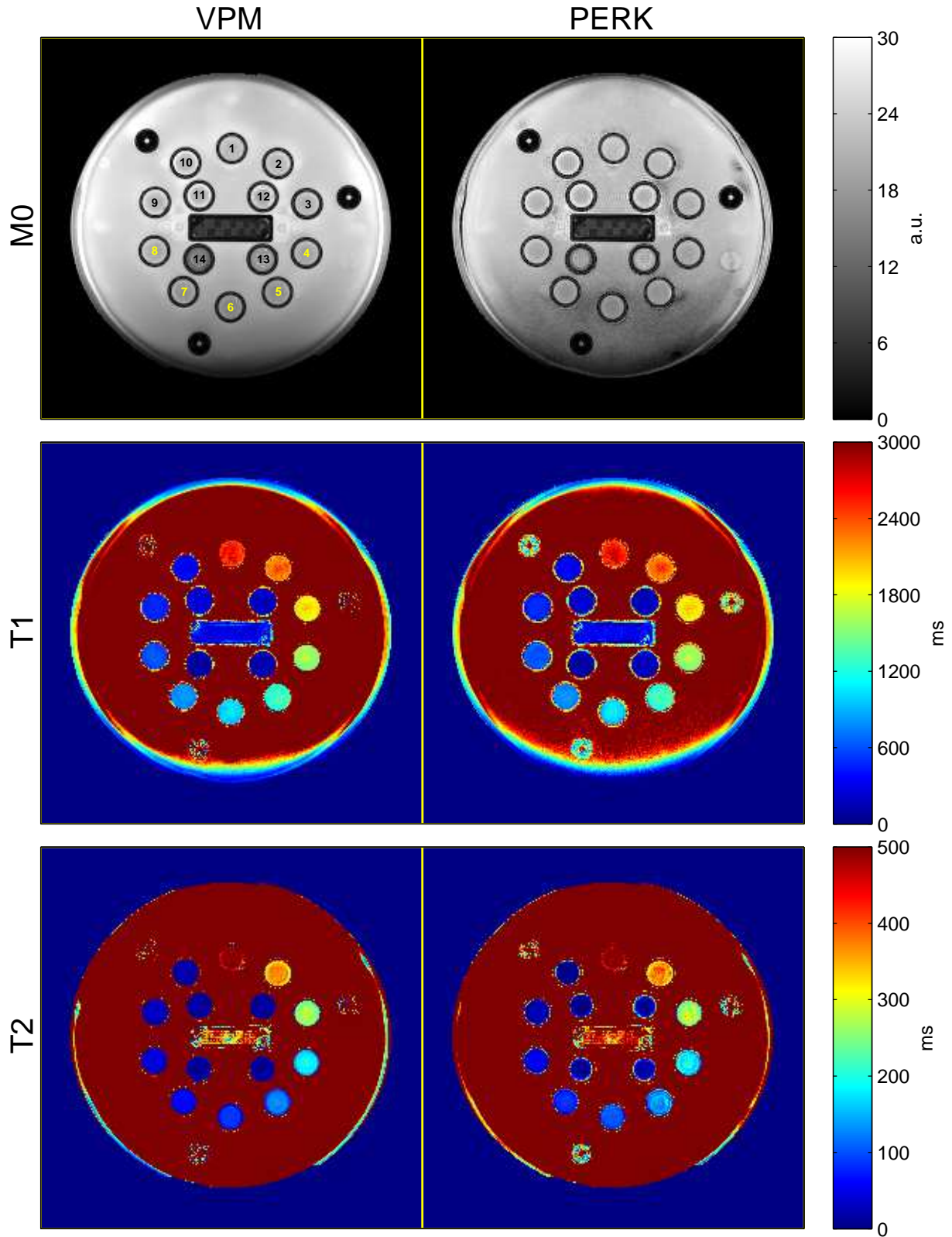


Fig. S.7: More aggressively trained VPM and PERK  $M_0$ ,  $T_1$ ,  $T_2$  estimates in a quantitative phantom. Here the PERK estimator was trained with a sampling distribution whose support extended over less well identified  $T_1$ ,  $T_2$  values. Comparing with analogous images in Fig. S.5, PERK performance within vials 4-8 degrades, though in other vials performance clearly improves. Vials are enumerated and highlighted to correspond with markers and colored boxes in Fig. S.6.